DATA AND IMAGES AVAILABLE AT HTTP://WWW.ASTRO.PSU.EDU/USERS/NIEL/CDFS/CDFS-CHANDRA.HTML
Preprint typeset using LaTeX style emulateapj v. 10/09/06

THE *CHANDRA* DEEP FIELD-SOUTH SURVEY: 2 MS SOURCE CATALOGS

B. LUO,[1] F. E. BAUER,[2] W. N. BRANDT,[1] D. M. ALEXANDER,[3] B. D. LEHMER,[3] D. P. SCHNEIDER,[1] M. BRUSA,[4,5] A. COMASTRI,[6] A. C. FABIAN,[7] A. FINOGUENOV,[4,5] R. GILLI,[6] G. HASINGER,[4] A. E. HORNSCHEMEIER,[8] A. KOEKEMOER,[9] V. MAINIERI,[10] M. PAOLILLO,[11] P. ROSATI,[10] O. SHEMMER,[1] J. D. SILVERMAN,[12] I. SMAIL,[13] A. T. STEFFEN,[14] & C. VIGNALI[15]

Data and images available at http://www.astro.psu.edu/users/niel/cdfs/cdfs-chandra.html

ABSTRACT

We present point-source catalogs for the ≈ 2 Ms exposure of the *Chandra* Deep Field-South (CDF-S); this is one of the two most-sensitive X-ray surveys ever performed. The survey covers an area of ≈ 436 arcmin^2 and reaches on-axis sensitivity limits of $\approx 1.9 \times 10^{-17}$ and $\approx 1.3 \times 10^{-16}$ ergs cm^{-2} s^{-1} for the 0.5–2.0 and 2–8 keV bands, respectively. Four hundred and sixty-two X-ray point sources are detected in at least one of three X-ray bands that were searched; 135 of these sources are new compared to the previous ≈ 1 Ms CDF-S detections. Source positions are determined using centroid and matched-filter techniques; the median positional uncertainty is $\approx 0\farcs36$. The X-ray–to–optical flux ratios of the newly detected sources indicate a variety of source types; $\approx$55% of them appear to be active galactic nuclei while $\approx$45% appear to be starburst and normal galaxies. In addition to the main *Chandra* catalog, we provide a supplementary catalog of 86 X-ray sources in the ≈ 2 Ms CDF-S footprint that was created by merging the ≈ 250 ks Extended *Chandra* Deep Field-South with the CDF-S; this approach provides additional sensitivity in the outer portions of the CDF-S. A second supplementary catalog that contains 30 X-ray sources was constructed by matching lower significance X-ray sources to bright optical counterparts ($R < 23.8$); the majority of these sources appear to be starburst and normal galaxies. The total number of sources in the main and supplementary catalogs is 578. *R*-band optical counterparts and basic optical and infrared photometry are provided for the X-ray sources in the main and supplementary catalogs. We also include existing spectroscopic redshifts for 224 of the X-ray sources. The average backgrounds in the 0.5–2.0 and 2–8 keV bands are 0.066 and 0.167 counts Ms^{-1} pixel^{-1}, respectively, and the background counts follow Poisson distributions. The effective exposure times and sensitivity limits of the CDF-S are now comparable to those of the ≈ 2 Ms *Chandra* Deep Field-North (CDF-N). We also present cumulative number counts for the main catalog and compare the results to those for the CDF-N. The soft-band number counts for these two fields agree well with each other at fluxes higher than $\approx 2 \times 10^{-16}$ ergs cm^{-2} s^{-1}, while the CDF-S number counts are up to ≈ 25% smaller than those for the CDF-N at fluxes below $\approx 2 \times 10^{-16}$ ergs cm^{-2} s^{-1} in the soft band and $\approx 2 \times 10^{-15}$ ergs cm^{-2} s^{-1} in the hard band, suggesting small field-to-field variations.

Subject headings: cosmology: observations — diffuse radiation — galaxies:active — surveys — X-rays: galaxies

1. INTRODUCTION

One of the greatest successes of the *Chandra X-Ray Observatory* (*Chandra*) has been the characterization of the sources creating the 0.5–8 keV cosmic X-ray background (CXRB), and the deepest *Chandra* surveys form a central part of this effort. The two deepest *Chandra* surveys, the *Chandra* Deep Field-North and *Chandra* Deep Field-South (CDF-N and CDF-S, jointly CDFs; see Brandt & Hasinger 2005 for a review), have each detected hundreds of X-ray sources over ≈ 450 arcmin^2 areas with enormous multiwavelength observational investments. They have measured the highest sky density of accreting supermassive black holes (SMBHs) to date and have also enabled novel X-ray studies of starburst and normal galaxies, groups and clusters of galaxies, large-scale structures in the distant universe, and Galactic stars.

As part of an effort to create still deeper X-ray surveys, we proposed for substantial additional exposure on the CDF-S during *Chandra* Cycle 9. The CDF-S has superb and improving coverage at optical, infrared, and radio wavelengths; it will continue to be a premiere multiwavelength deep-survey field for the coming decades as additional large facilities are deployed in the southern hemisphere. Furthermore, owing to the 1 Ms of *Chandra* exposure already available (Giacconi et al. 2002, hereafter G02), the CDF-S is a natural field to observe more sensitively. Although our proposal was not approved in the peer review, subsequently 1 Ms of Di-

[1] Department of Astronomy & Astrophysics, 525 Davey Lab, The Pennsylvania State University, University Park, PA 16802, USA
[2] Columbia Astrophysics Laboratory, Columbia University, Pupin Laboratories, 550 W. 120th St., New York, NY 10027, USA
[3] Department of Physics, Durham University, Durham, DH1 3LE, UK
[4] Max-Planck-Institut für Extraterrestrische Physik, Giessenbachstrasse, D-85748 Garching b. München, Germany
[5] University of Maryland, Baltimore County, 1000 Hilltop Circle, Baltimore, MD 21250, USA
[6] INAF—Osservatorio Astronomico di Bologna, Via Ranzani 1, Bologna, Italy
[7] Institute of Astronomy, Madingley Road, Cambridge, CB3 0HA, UK
[8] Laboratory for X-ray Astrophysics, NASA Goddard Space Flight Center, Code 662, Greenbelt, MD 20771, USA
[9] Space Telescope Science Institute, 3700 San Martin Drive, Baltimore, MD 21218, USA
[10] European Southern Observatory, Karl-Schwarzschild-Strasse 2, Garching, D-85748, Germany
[11] Dipartimento de Scienze Fisiche, Università di Napoli, Via Cinthia, 80126 Napoli, Italy
[12] ETH Zurich, Institute of Astronomy, Department of Physics, Wolfgang-Pauli-Strasse 16, 8093 Zurich, Switzerland
[13] Institute of Computational Cosmology, Durham University, Durham, DH1 3LE, UK
[14] Spitzer Science Center, California Institute of Technology, Mail Code 220-6, 1200 East California Boulevard, Pasadena, CA 91125, USA
[15] Universitá di Bologna, Via Ranzani 1, Bologna, Italy

rector's Discretionary Time was allocated for deeper CDF-S observations. The allocated observations were successfully executed in 2007 September, October and November, raising the CDF-S exposure to ≈ 2 Ms and improving its sensitivity to be comparable to that of the CDF-N (e.g., Alexander et al. 2003, hereafter A03). Additional sky coverage at such flux levels is critically important as it substantially improves the statistical sample sizes of the faintest X-ray sources and also allows a basic assessment of the effects of cosmic variance. Furthermore, approximately doubling the exposure on previously detected sources substantially improves the constraints on their positions, spectral properties, and variability properties.

In this paper, we present up-to-date *Chandra* source catalogs and data products derived from the full ≈ 2 Ms CDF-S data set along with details of the observations, data processing, and technical analysis. Detailed subsequent investigations and scientific interpretation of the new CDF-S sources will be presented in future papers, e.g., studies of heavily obscured and Compton-thick active galactic nuclei (AGNs), high-redshift AGNs, AGN spectra and variability, starburst and normal galaxies, and clusters and groups of galaxies. In §2 we describe the observations and data reduction, and in §3 we present the main and supplementary point source catalogs and describe the methods used to create these catalogs. In §4 we estimate the background and sensitivity across the survey region. We also present basic number-count results for point sources in §5. We summarize in §6.

The Galactic column density along the line of sight to the CDF-S is remarkably low: $N_{\rm H} = 8.8 \times 10^{19}$ cm^{-2} (e.g., Stark et al. 1992). The coordinates throughout this paper are J2000. A $H_0 = 70$ km s^{-1} Mpc^{-1}, $\Omega_{\rm M} = 0.3$, and $\Omega_\Lambda = 0.7$ cosmology is adopted.

2. OBSERVATIONS AND DATA REDUCTION

2.1. *Observations and Observing Conditions*

The CDF-S consists of 23 separate observations described in Table 1. The ≈ 1 Ms catalogs for the first 11 observations taken between 1999 October 14 and 2000 December 23 were presented in G02 and A03. Note that observation 581 (1999 October 14) was excluded from the data reduction and is not listed in Table 1 due to telemetry saturation and other problems. The second ≈ 1 Ms exposure consisted of 12 observations taken between 2007 September 20 and 2007 November 4.

The Advanced CCD Imaging Spectrometer imaging array (ACIS-I; Garmire et al. 2003) was used for all of the *Chandra* observations. The ACIS-I is composed of four 1024×1024 pixel CCDs (CCDs I0–I3), covering a field of view of $16\farcm9 \times 16\farcm9$ ($\approx$285 arcmin^2), and the pixel size of the CCDs is $\approx 0\farcs492$. The focal-plane temperature was -110°C for observations 1431-0 and 1431-1, and -120°C for the others. The 12 new observations were taken in Very Faint mode to improve the screening of background events and thus increase the sensitivity of ACIS in detecting faint X-ray sources (Vikhlinin 2001).

The background light curves for all 23 observations were inspected using EVENT BROWSER in the Tools for ACIS Real-time Analysis (TARA; Broos et al. 2000) software package. Aside from a mild flare during observation 1431-0 (factor of ≈ 3 increase for ≈ 5 ks), all data sets are free from significant flaring, and the background is stable within $\approx$20% of typical quiescent *Chandra* values. After filtering on good-time intervals and removing the one mild flare, we are left with 1.911 Ms of total exposure time for the 23 observations.

Because of the differences in pointings and roll angles for the individual exposures, the total region covered by the entire CDF-S is 435.6 arcmin^2, considerably larger than the ACIS-I field of view. Combining the 23 observations, the average aim point (weighted by exposure time) is $\alpha_{\rm J2000.0} = 03^{\rm h}32^{\rm m}28\fs80$, $\delta_{\rm J2000.0} = -27^\circ48'23\farcs0$.

2.2. *Data Reduction*

The basic archive data products were processed with the *Chandra* X-ray Center (CXC) pipeline software versions listed in Table 1. The reduction and analysis of the data used *Chandra* Interactive Analysis of Observations (CIAO) tools whenever possible[16]; however, custom software, including the TARA package, was also used. Each observation was reprocessed using the CIAO tool ACIS_PROCESS_EVENTS, to correct for the radiation damage sustained by the CCDs during the first few months of *Chandra* operations using a Charge Transfer Inefficiency (CTI) correction procedure (Townsley et al. 2000, 2002) [17], to remove the standard pixel randomization which blurs the *Chandra* point spread function (PSF), and to apply a modified bad-pixel file as detailed below.

One important deviation from the standard *Chandra* reduction procedure outlined by the CXC is implementation of a stripped-down bad-pixel file. We note that the standard bad-pixel file supplied with all *Chandra* data currently excludes $\approx$ 6–7% of the total effective area on front-illuminated devices (e.g., ACIS-I). A large fraction of the bad-pixel locations identified in this file, however, appear to be flagged solely because they show a few extra events (per Ms) almost exclusively below 0.5–0.7 keV.[18] Good events with energies above 0.7 keV that fall on these bad pixels are likely to be perfectly acceptable for source searching, as well as for photometry and spectral analysis albeit with a few mild caveats regarding misinterpretation. Rather than reject all events falling on such columns, we instead adopted a procedure to only exclude events below a row-dependent energy of 0.5–0.7 keV. [19] To this end, we generated a stripped-down bad-pixel file, only selecting obvious bad columns and pixels above 1 keV; this excluded $\approx 1.5\%$ of the total effective area on front-illuminated devices. Once the entire ≈ 2 Ms data set was combined, we isolated "hot" soft columns as those where the total number of events with energies below 0.7 keV was 5σ or more above the mean. We then rejected any events in those columns that fell below a row-dependent 0.5–0.7 keV; this removed 1% of all events.

Through inspection of the data in CCD coordinates, we additionally discovered that the CXC-preferred CIAO tool ACIS_RUN_HOTPIX failed to flag a substantial number of obvious cosmic-ray afterglows ($\sim$100–200 per observation, depending on exposure length), elevating the overall background and, in egregious cases, leaving afterglows to be

[16] See http://cxc.harvard.edu/ciao/ for details on CIAO.

[17] Note that the CXC CTI correction procedure is only available for -120°C data; thus we did not CTI-correct observations 1431-0 and 1431-1.

[18] See http://cxc.harvard.edu/cal/Acis/Cal_prods/badpix/index.html

[19] The energy range of 0.5–0.7 keV and frequency of occurrence were verified by visual inspection of such columns in our ≈ 2 Ms data set. We found that such "hot" soft columns were not clearly seen in any individual observations. The upper energy bound appears to vary as a function of distance from the readout edge of the front-illuminated CCDs, such that rows closest to the readout edge only have extra events below $\approx$0.5 keV, while those furthest away have extra events extending up to $\approx$0.7 keV.

mistaken as real sources. This problem appeared to be worse for Faint mode data, presumably because the additional 5×5 screening applied in Very Faint mode rejects the strongest afterglows (Vikhlinin 2001). To remedy this situation, we reverted to using the more stringent ACIS_DETECT_AFTERGLOW algorithm on all of our data. Notably, none of our sources has a count rate high enough that ACIS_DETECT_AFTERGLOW would reject true source counts, which we verified by inspection of events flagged by this routine. Even ACIS_DETECT_AFTERGLOW failed to reject all afterglows, and thus we created custom software to remove many remaining faint afterglows from the data. Working in CCD coordinates, we removed additional faint afterglows with three or more total counts occuring within 20 s (or equivalently 6 consecutive frames). In total, we removed 229 total events associated with afterglows. In all cases, we inspected the data set and found that such flagged events were isolated and not associated with apparent legitimate X-ray sources.

3. PRODUCTION OF THE POINT-SOURCE CATALOGS

The production of the point-source catalogs largely followed the procedure described in §3 of A03. The main differences in the catalog-production procedure used here are the following:

1. Our main *Chandra* catalog includes sources detected by running WAVDETECT (Freeman et al. 2002) at a false-positive probability threshold of 10^{-6}, less conservative than the 10^{-7} value adopted by A03. Even with this revised threshold, we expect the fraction of false sources to be small; see §3.2 for details.

2. Additional sensitivity can be obtained by merging the $\approx$ 250 ks Extended *Chandra* Deep Field-South (E-CDF-S; Lehmer et al. 2005, hereafter L05) with the $\approx$ 2 Ms CDF-S. An additional 86 X-ray sources were detected with this approach. These sources are presented in a supplementary catalog described in §3.3.2.

3.1. *Image and Exposure Map Creation*

We registered the observations in the following manner. WAVDETECT was run on each individual cleaned image to generate an initial source list. Centroid positions for each detected source were determined using the reduction tool ACIS EXTRACT (AE; Broos et al. 2000).[20] The observations were registered to a common astrometric frame by matching X-ray centroid positions to optical sources detected in deep *R*-band images taken with the Wide Field Imager (WFI) of the MPG/ESO telescope at La Silla (see §2 of Giavalisco et al. 2004). The matching was performed using the CIAO tools REPROJECT_ASPECT and WCS_UPDATE adopting a $3''$ matching radius and a residual rejection limit [21] of $0\farcs6$; 50–100 sources were typically used in each observation for the final astrometric solution. The tool WCS_UPDATE applied linear translations ranging from $0\farcs05$ to $0\farcs34$, rotations ranging from $-0\fdg239$ to $0\fdg009$, and scale stretches ranging from 0.999563 to 1.000714; individual registrations are accurate to $\approx 0\farcs3$. All of the observations were then reprojected to the frame of observation 2406, since this data set required the smallest translation to align it with the optical astrometric frame.

[20] The ACIS EXTRACT software can be accessed from http://www.astro.psu.edu/xray/docs/TARA/ae_users_guide.html

[21] This is a parameter used in WCS_UPDATE to remove source pairs based on pair positional offsets.

We constructed images using the standard *ASCA* grade set (*ASCA* grades 0, 2, 3, 4, 6) for three standard bands: 0.5–8.0 keV (full band; FB), 0.5–2.0 keV (soft band; SB), and 2–8 keV (hard band; HB). Figure 1 shows the full-band raw image. Exposure maps in the three standard bands were created following the basic procedure outlined in §3.2 of Hornschemeier et al. (2001) and were normalized to the effective exposures of a source located at the average aim point. Briefly, this procedure takes into account the effects of vignetting, gaps between the CCDs, bad-column filtering, bad-pixel filtering, and the spatially dependent degradation in quantum efficiency due to contamination on the ACIS optical-blocking filters. A photon index of $\Gamma = 1.4$ was assumed in creating the exposure maps, which is approximately the slope of the X-ray background in the 0.5–8.0 keV band (e.g., Marshall et al. 1980; Gendreau et al. 1995; Hasinger et al. 1998). We show the full-band exposure map in Figure 2. Using the full-band exposure map, we calculated the survey solid angle as a function of the minimum full-band effective exposure; the result is plotted in Figure 3. Approximately 56% and 42% of the CDF-S field has a full-band effective exposure greater than 1 Ms and 1.5 Ms, respectively, with a maximum effective exposure of ≈ 1.884 Ms (note this is slightly smaller than the 1.911 Ms total exposure since the aim points of all the *Chandra* observations were not exactly the same). The survey solid angles are comparable to those of the $\approx$ 2 Ms CDF-N (A03; dashed curve in Fig. 3).

Adaptively smoothed images were created using the CIAO tool CSMOOTH on the raw images. Exposure-corrected smoothed images were then constructed following §3.3 of Baganoff et al. (2003). We show in Figure 4 a color composite of the exposure-corrected smoothed images in the 0.5–2.0 keV (*red*), 2–4 keV (*green*), and 4–8 keV (*blue*) bands. Source searching was performed using only the raw images, while many of the detected X-ray sources are shown more clearly in the adaptively smoothed images.

3.2. *Point-Source Detection*

Point-source detection was performed in each of the three standard bands with WAVDETECT using a "$\sqrt{2}$ sequence" of wavelet scales (i.e., 1, $\sqrt{2}$, 2, $2\sqrt{2}$, 4, $4\sqrt{2}$, 8, $8\sqrt{2}$, and 16 pixels). The criterion for source detection is that a source must be found with a given false-positive probability threshold in at least one of the three standard bands. For the main *Chandra* source catalog discussed in §3.3.1, the false-positive probability threshold in each band was set to 1×10^{-6}.

If we conservatively consider the three images searched to be independent, $\approx$18 false detections are expected in the main *Chandra* source catalog for the case of a uniform background. However, this false-source estimate is conservative, since a single pixel usually should not be considered a source-detection cell, particularly at large off-axis angles (WAVDETECT suppresses fluctuations on scales smaller than the PSF). As quantified in §3.4.1 of A03, the number of false-sources is likely $\approx$2–3 times less than our conservative estimate. We also provide additional source-significance information by running WAVDETECT using false-positive probability thresholds of 1×10^{-7} and 1×10^{-8}. These results are presented in §3.3.1, which can be utilized to perform more conservative source screening if desired.

3.3. *Point-Source Catalogs*

3.3.1. *Main Chandra Source Catalog*

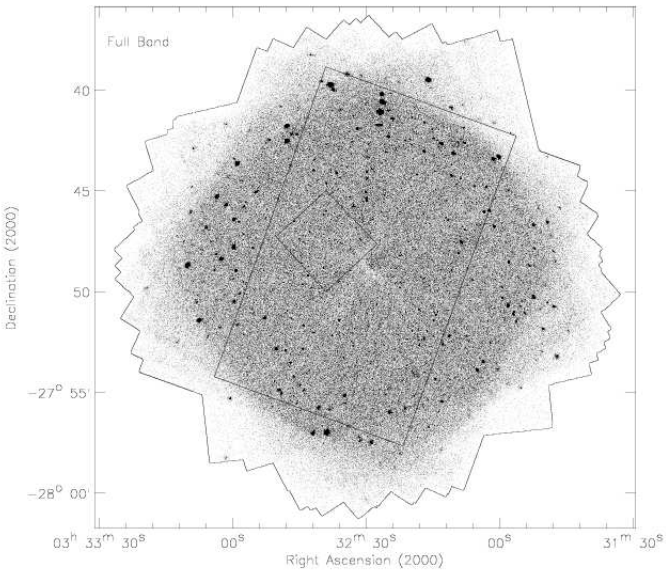

FIG. 1.— Full-band (0.5–8.0 keV) raw image of the ≈2 Ms CDF-S. The gray scales are linear. The apparent scarcity of sources near the field center is largely due to the small PSF at that location (see Figs. 4 and 10 for clarification). The black outline surrounding the image indicates the extent of all the CDF-S observations. The large rectangle indicates the GOODS-S (Giavalisco et al. 2004) region, and the central square indicates the *Hubble* Ultra Deep Field (UDF; Beckwith et al. 2006) region. The cross near the center of the images indicates the average aim point, weighted by exposure time (see Table 1).

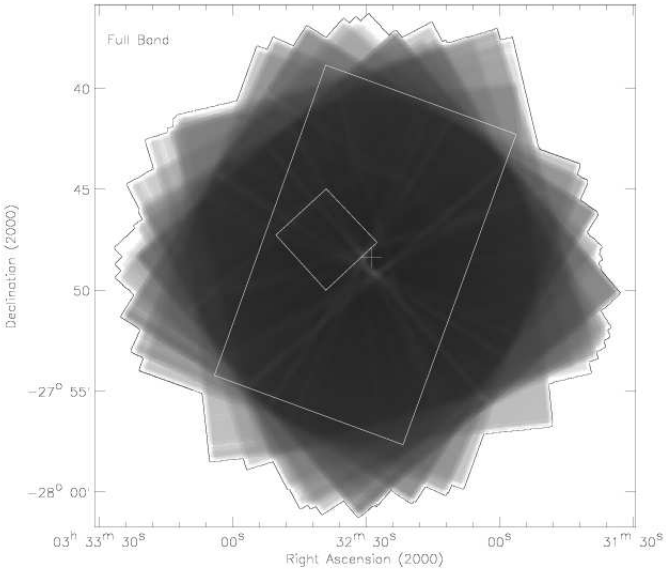

FIG. 2.— Full-band (0.5–8.0 keV) exposure map of the ≈ 2 Ms CDF-S. The darkest areas represent the highest effective exposure times (the maximum value is 1.884 Ms). The gray scales are logarithmic. The regions and the cross symbol have the same meaning as those in Fig. 1.

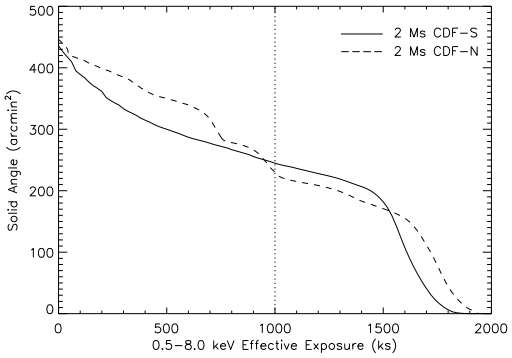

FIG. 3.— Amount of survey solid angle having at least a given amount of full-band effective exposure for the ≈ 2 Ms CDF-S (*solid curve*). The maximum exposure is ≈ 1.884 Ms. The vertical dotted line shows an effective exposure of 1 Ms. About 245 arcmin^2 (≈ 56%) of the CDF-S survey area has > 1 Ms effective exposure. Corresponding data from the ≈ 2 Ms CDF-N (A03) are plotted as a dashed curve for comparison.

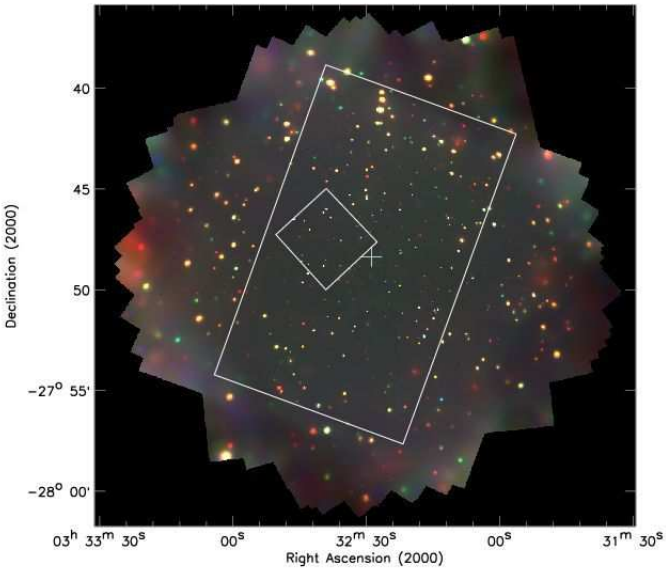

FIG. 4.— *Chandra* "false-color" image of the ≈2 Ms CDF-S. This image is a color composite of the exposure-corrected adaptively smoothed images in the 0.5–2.0 keV (*red*), 2–4 keV (*green*), and 4–8 keV (*blue*) bands. The apparent smaller size and lower brightness of sources near the field center is due to the small PSF at that location. The regions and the cross symbol have the same meaning as those in Fig. 1.

The source lists resulting from the WAVDETECT runs discussed in §3.2 with false-positive probability threshold of 1×10^{-6} were merged to create the main point-source catalog presented in Table 2, which consists of 462 point sources. Whenever possible, we have quoted the position determined in the full band; when a source is not detected in the full band, we used, in order of priority, the soft-band position or hard-band position. For cross-band matching, we used a matching radius of $2\farcs5$ for sources within $6'$ of the average aim point and $4\farcs0$ for larger off-axis angles. These matching radii were chosen by inspecting histograms showing the number of matches obtained as a function of angular separation (e.g., see §2 of Boller et al. 1998); the mismatch probability is $\lesssim 1\%$ over the entire field. A few mismatches near the edge of the

field were removed through visual inspections.

We improved the WAVDETECT source positions using the centroid and matched-filter positions generated with AE. The centroid is simply the mean position of all events within the AE extraction region, while the matched-filter position is the position found by correlating the full-band image in the vicinity of each source with a combined PSF. The combined PSF is produced by combining the "library" PSF of a source for each observation, weighted by the number of detected counts.[22] This technique takes into account the fact that, due to the complex PSF at large off-axis angles, the X-ray source position is not always located at the peak of the X-ray emission. The WAVDETECT, centroid, and matched-filter techniques provide comparable accuracy on-axis, while the matched-filter technique performs better off-axis. We chose the matched-filter positions as our default, and then visually inspected each source. When the adopted position appeared to deviate from the apparent center of the source by more than $0\farcs1$, we modified the position manually such that it was visually consistent with the apparent center.

We refined the absolute X-ray source positions by matching the X-ray sources in the main *Chandra* catalog to the WFI *R*-band optical sources (see §3.1). There are $\approx 30\,000$ optical sources across the CDF-S field, which have accurate positions with positional error $\Delta_o \approx 0\farcs1$.[23] We selected relatively bright optical sources with AB magnitudes $R \leq 24$ ($\approx 5\,500$ sources), and matched them to the X-ray sources using a $2\farcs5$ matching radius. There are eight cases where one X-ray source has two optical counterparts. The *R*-band magnitudes of the two counterparts differ by less than one in all cases, and thus we selected the closer one as the most-probable counterpart. We also visually inspected the optical counterparts and, for purposes of positional checking, only keep those sources that are point-like or slightly extended; ten extended sources were removed. Under these criteria, 229 X-ray sources have bright optical counterparts. We estimated the expected number of false matches by manually shifting the X-ray source coordinates in right ascension and declination by $5\farcs0$ (both positive and negative shifts) and recorrelating with the optical sources. On average, the number of false matches is ≈ 35 ($\approx 15\%$), and the median offset of these false matches is $\approx 1\farcs71$. By comparing the X-ray and optical source positions, we found small shift and plate-scale corrections. These corrections have been applied to the positions of all the X-ray sources in the main and supplementary catalogs, resulting in small ($< 0\farcs2$) astrometric shifts.

We investigated the accuracy of the X-ray source positions using these 229 X-ray detected bright optical sources. Figure 5 shows the positional offset between the X-ray sources and their optical counterparts as a function of the off-axis angle. The median offset is $\approx 0\farcs36$. However, there are clear off-axis angle and source-count dependencies. The off-axis angle dependence is due to the degradation of the *Chandra* PSF at large off-axis angles, while the count dependence is due to the difficulty of finding the centroid of a faint X-ray source. Simulations have shown that the offsets of WAVDETECT positions appear to increase exponentially with off-axis angle and decrease with the number of source counts in a power-law form (e.g., Kim et al. 2007). Based on Figure 5 and taking into account the probability of false matches, we

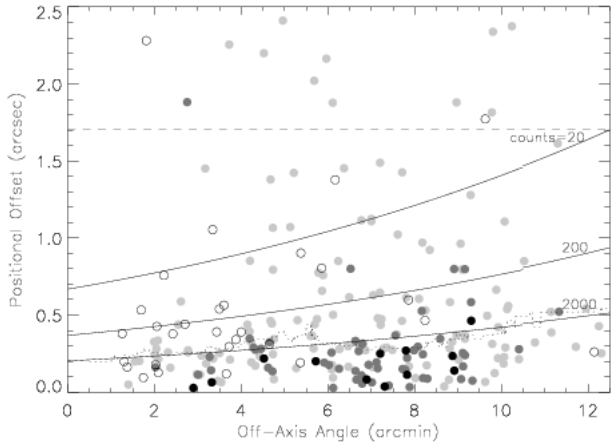

FIG. 5.— Positional offset vs. off-axis angle for sources in the main *Chandra* catalog that were matched to WFI *R*-band optical sources with AB magnitude $R \leq 24$ to within $2\farcs5$. Black, dark gray, light gray, and open circles represent *Chandra* sources with ≥ 2000, ≥ 200, ≥ 20, and < 20 counts in the energy band where the source position was determined, respectively. The dotted curve shows the running median of all sources in bins of $2'$. The median offset of the expected false matches ($\approx 1\farcs71$) is indicated by the dashed line. These data were used to derive the $\approx 85\%$ confidence-level positional uncertainties of the X-ray sources in the main catalog; see eq. (1). Three solid curves indicate the $\approx 85\%$ confidence-level positional uncertainties for sources with counts of 20, 200 and 2000. The number of black, dark-gray, and light-gray circles lying below/above their corresponding solid curves are 11/1, 48/4 and 116/20, respectively. Note that sources with more than 20 or 200 counts will have expected positional uncertainties smaller than those indicated by the corresponding solid curves.

derived an empirical relation for the positional uncertainties of the X-ray sources in our sample, which is

$$\log \Delta_X = 0.0326\theta - 0.2595 \log C + 0.1625\,, \qquad (1)$$

where Δ_X is the positional uncertainty in arcseconds, θ the off-axis angle in arcminutes, and C the source counts in the energy band where the source position was determined. We set an upper limit of 2000 on C as the positional accuracy does not improve significantly beyond that level. Positional uncertainties for $C = 20$, 200, and 2000 are shown in Figure 5. The stated positional uncertainties are for the $\approx 85\%$ confidence level, and are smaller than the WAVDETECT positional errors, especially at large off-axis angles, because of our positional refinement described above. A few sources in Figure 5 have unexpectedly large positional offsets; they could be false matches.[24] There is also the possibility that a few of them are off-nuclear X-ray sources (e.g., Hornschemeier et al. 2004; Lehmer et al. 2006). Figure 6 shows the distributions of the positional offsets in four bins of different X-ray positional uncertainties, as well as the expected numbers of false matches assuming a uniform spatial distribution of the $R \leq 24$ optical sources. These histograms illustrate clearly the reliability of our positional error estimates calculated using equation (1).

The main *Chandra* X-ray source catalog is presented in Table 2, with the details of the columns given below.

1. Column 1: the source number. Sources are listed in order of increasing right ascension.

[22] The PSFs are taken from the CXC PSF library; see http://cxc.harvard.edu/ciao/dictionary/psflib.html.

[23] See http://archive.stsci.edu/pub/hlsp/goods/v1/h_goods_v1.0_rdm.html.

[24] For example, the source with > 200 counts and a positional offset of $\approx 1\farcs9$ in Figure 5 is source "289" in the main *Chandra* catalog (see Table 2). This source does not have any optical counterpart after adopting a more appropriate matching radius, as shown in the catalog.

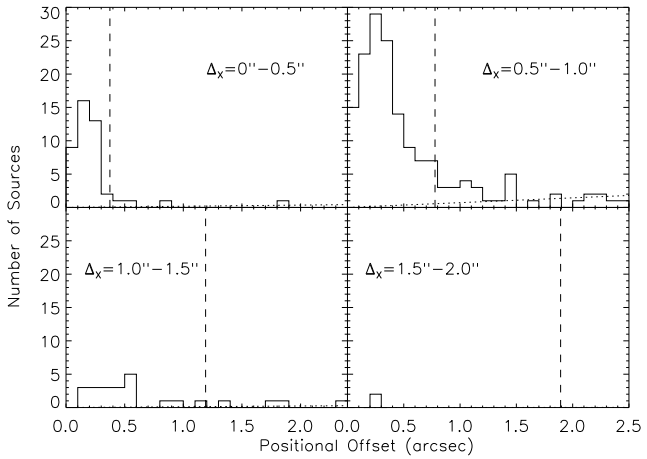

FIG. 6.— Histograms showing the distributions of positional offset for sources in the main *Chandra* catalog that were matched to WFI *R*-band optical sources with $R \leq 24$ to within $2\farcs5$. X-ray sources were divided into four bins based on their positional uncertainties estimated using eq. (1): $0\farcs0$–$0\farcs5$, $0\farcs5$–$1\farcs0$, $1\farcs0$–$1\farcs5$, and $1\farcs5$–$2\farcs0$. The vertical dashed line indicates the median positional uncertainty for X-ray sources in each bin. Dotted lines show how many random $R \leq 24$ optical sources are expected as a function of the positional offset. Less than 20% of the optical counterparts lie beyond the median X-ray positional uncertainties in all cases.

2. Columns 2 and 3: the right ascension and declination of the X-ray source, respectively. These positions have been determined following the procedure described above. To avoid truncation error, we quote the positions to higher precision than in the International Astronomical Union (IAU) registered names beginning with the acronym "CXO CDFS".

3. Column 4: the $\approx 85\%$ confidence-level positional uncertainty in arcseconds. As shown above, the positional uncertainty depends on off-axis angle and the number of detected counts, and is estimated following equation (1). The minimum positional uncertainty is $\approx 0\farcs23$ for sources in the main catalog, and the maximum value is $\approx 1\farcs90$.

4. Column 5: the off-axis angle of the X-ray source in arcminutes. This is calculated using the source position given in columns 2 and 3 and the average aim point of the CDF-S (see Table 1).

5. Columns 6–14: the source counts and the corresponding 1σ statistical errors (Gehrels 1986) or the upper limits on source counts for the three standard bands, respectively. The entries have not been corrected for vignetting. Source counts and statistical errors have been calculated using circular-aperture photometry; extensive testing has shown that this method is more reliable than the WAVDETECT photometry (e.g., Brandt et al. 2001; A03). The circular aperture was centered at the position given in columns 2 and 3 for all bands. We have also computed photometry using AE, and the results are in good agreement with this circular-aperture photometry.

   The local background is determined in an annulus outside of the source-extraction region. The mean number of background counts per pixel is calculated from a Poisson model using n_1/n_0, where n_0 is the number of pixels with 0 counts and n_1 is the number of pixels with 1 count (e.g., A03). By ignoring all pixels with more than 1 count, this technique is robust against background contamination from sources. The principal requirement for using this Poisson-model technique is that the background counts are low and follow a Poisson distribution; we show in §4 that the background of the ≈ 2 Ms exposure meets this criterion. We note that the background estimation is problematic for several sources which are located close to bright sources or near the edge of the survey field where there is a strong gradient in exposure time. For each of these sources, we have measured its background counts in the background maps described in §4, using an annulus outside of the source-extraction region. Note that when constructing the background maps, we filled in the masked regions with a local background assuming a probability distribution; thus small additional uncertainties could be introduced during this process and will be carried on to the background estimation here. There are 17 such sources and they are marked with "B" in column 49 of Table 2. The net number of source counts is calculated by subtracting the background counts from the source counts.

   For sources with fewer than 1000 full-band counts, we have chosen the aperture radii based on the encircled-energy function of the *Chandra* PSF as determined using the CXC's MKPSF software (Feigelson et al. 2000; Jerius et al. 2000). In the soft band, where the background is lowest, the aperture radius was set to the 95% encircled-energy radius of the PSF. In the full and hard bands, the 90% encircled-energy radius of the PSF was used. Appropriate aperture corrections were applied to the source counts by dividing the extracted source counts by the encircled-energy fraction for which the counts were extracted.

   For sources with more than 1000 full-band counts, systematic errors in the aperture corrections often exceed the expected errors from photon statistics when the apertures described in the previous paragraph are used. Therefore, for such sources we used larger apertures to minimize the importance of the aperture corrections; this is appropriate since these bright sources dominate over the background. We set the aperture radii to be twice the 90% encircled-energy full-band radii and inspected these sources to verify that the measurements were not contaminated by neighboring objects. No aperture corrections were applied to these sources.

   Manual correction of the source photometry was performed for sources having overlapping PSFs. We manually separated 18 close doubles and 4 close triples, and these sources are flagged with "S" in column 49 of Table 2.

   We have performed several consistency tests to verify the quality of the photometry. For example, we have checked that the sum of the counts measured in the soft and hard bands does not differ from the counts measured in the full band by an amount larger than that expected from measurement error. Systematic errors that arise from differing full-band counts and soft-band plus hard-band counts are estimated to be $\lesssim 4\%$.

   When a source is not detected in a given band, an upper limit is calculated; upper limits are indicated as a "−1.00" in the error columns. All upper limits are de-

termined using the circular apertures described above. When the number of counts in the aperture is ≤ 10, the upper limit is calculated using the Bayesian method of Kraft et al. (1991) for 99% confidence. The uniform prior used by these authors results in fairly conservative upper limits (see Bickel 1992), and other reasonable choices of priors do not materially change our scientific results. For larger numbers of counts in the aperture, upper limits are calculated at the 3σ level for Gaussian statistics.

6. Columns 15 and 16: the right ascension and declination of the optical counterpart, which was obtained by matching the X-ray source positions (columns 2 and 3) to WFI *R*-band source positions using a matching radius that is 1.5 times the quadratic sum of the positional errors of the X-ray and optical sources (i.e., $r_{\rm m} = 1.5\sqrt{\Delta_{\rm x}^2 + \Delta_{\rm o}^2}$). This matching radius was chosen to provide a large number of optical counterparts without introducing too many false matches. The WFI *R*-band observations have a 5σ limiting AB magnitude of 27.3 over the entire CDF-S field. For 4 sources (our sources "74", "283", "328", and "431") that have more than one optical match, the magnitude difference between the counterparts is less than three in all cases, and therefore the source with the smallest offset was selected as the most-probable counterpart. Using these criteria, 344 ($\approx 74\%$) of the sources have optical counterparts. Sources with no optical counterparts have these right ascension and declination values set to "00 00 00.00" and "–00 00 00.0". We tested the reliability of the matching by shifting the X-ray source coordinates and recorrelating with the optical sources. The matching is reliable (false-match probability $\lesssim 8\%$) to $R \approx 24$. The false-match probability rises to $\approx 18\%$, $\approx 27\%$, and $\approx 35\%$ at $R \approx 25$, 26, and 27, respectively.

7. Column 17: the measured offset between the optical and X-ray sources in arcseconds. Sources with no optical counterparts have a value set to "–1.00". The offsets for all matches are below $2\farcs0$.

8. Column 18: the *R*-band AB magnitude of the optical counterpart. Sources with no optical counterparts have a value set to "–1.00".

9. Columns 19 and 20: the corresponding source number and *i*-band AB magnitude from the GOODS-S v2.0 *i*-band source catalog.[25] We matched the positions of the optical counterparts (see columns 15 and 16) to the GOODS-S source positions using a matching radius of $0\farcs5$. In 6 cases (our sources "88", "120", "135", "155", "313", and "322") where there is more than one GOODS-S source matching to an optical counterpart, we selected the GOODS-S source with the smallest offset as the most-probable match. 218 matches were found for the 344 optical counterparts; note that the GOOD-S field does not cover the whole CDF-S. By shifting the coordinates of the optical counterparts and recorrelating with the GOODS-S sources, we estimated the false-match probability to be $\lesssim 5\%$. The GOODS-S *i*-band observations have a 5σ limiting AB magnitude of 28.5. The *i*-band magnitude is the SExtractor (Bertin & Arnouts 1996) corrected isophotal magnitude. Sources with no GOODS-S match have these two columns set to "–1" and "–1.00", respectively.

10. Columns 21 and 22: the corresponding coordinate-based source name and *z*-band AB magnitude from the Galaxy Evolution from Morphologies and SEDs (GEMS) source catalog (Caldwell et al. 2008). We matched the positions of the optical counterparts (see columns 15 and 16) to the GEMS source positions using a matching radius of $0\farcs5$. In 1 case (our source "74") where there is more than one GEMS source matching to an optical counterpart, we selected the GEMS source with the smallest offset as the most-probable match. 297 matches were found for the 344 optical counterparts. By shifting the coordinates of the optical counterparts and recorrelating with the GEMS sources, we estimated the false-match probability to be $\lesssim 2\%$. The GEMS *z*-band observations have a 5σ limiting AB magnitude of 27.3 over the entire CDF-S field. The *z*-band magnitude is the SExtractor MAG_BEST magnitude. Sources with no GEMS match have these two columns set to "–1" and "–1.00", respectively.

11. Columns 23 and 24: the corresponding source number and K_s-band AB magnitude from the source catalog for the ESO/NTT SOFI survey of the CDF-S region.[26] We matched the positions of the optical counterparts (see columns 15 and 16) to the SOFI source positions using a matching radius of $0\farcs75$. 266 matches were found for the 344 optical counterparts. By shifting the coordinates of the optical counterparts and recorrelating with the SOFI sources, we estimated the false-match probability to be $\lesssim 1\%$. The SOFI K_s-band observations have a 5σ limiting AB magnitude of 23.0 over the entire CDF-S field. The K_s-band magnitude is the SExtractor corrected isophotal magnitude. Sources with no SOFI match have these two columns set to "–1" and "–1.00", respectively.

12. Columns 25 and 26: the corresponding source number and IRAC 5.8 μm flux density (f_{58}) from the *Spitzer* IRAC/MUSYC Public Legacy Survey in the E-CDF-S (SIMPLE) source catalog.[27] We matched the positions of the optical counterparts (see columns 15 and 16) to the SIMPLE source positions using a matching radius of $0\farcs75$. 306 matches were found for the 344 optical counterparts. By shifting the coordinates of the optical counterparts and recorrelating with the SIMPLE sources, we estimated the false-match probability to be $\lesssim 2\%$. The SIMPLE 5.8 μm observations have a 5σ limiting AB magnitude of 21.9–22.5 over the entire CDF-S field; the limiting magnitude is spatially dependent for SIMPLE. The 5.8 μm flux density is the aperture flux density in a $2\farcs0$ circular aperture, normalized to an AB magnitude zero point of 25. Note that an aperture correction of ≈ 1.5 was not applied to these fluxes; i.e., the aperture-corrected AB magnitude is $m({\rm AB}) = 25 - 2.5\log10(1.5 \times f_{58})$. Sources with no SIMPLE match have these two columns set to "–1" and "–1.00", respectively.

[25] See Giavalisco et al. (2004) and http://archive.stsci.edu/pub/hlsp/goods/catalog_r2/.

[26] See http://www.eso.org/sci/activities/projects/eis/surveys/summary_DPS.html.

[27] See http://ssc.spitzer.caltech.edu/legacy/simplehistory.html.

13. Columns 27 and 28: the corresponding spectroscopic redshift and the reference for the redshift. Secure spectroscopic redshifts were collected from Le Fèvre et al. (2004), Szokoly et al. (2004), Mignoli et al. (2005), Ravikumar et al. (2007), Popesso et al. (2008), and Vanzella et al. (2008), with the reference numbers of 1–6 in column 28, respectively. A matching radius of $0\farcs5$ was used when matching the optical counterparts (see columns 15 and 16) to the redshift catalogs. 190 of the 344 optical counterparts have redshift measurements. By shifting the coordinates of the optical counterparts and recorrelating with the redshift catalogs, we estimated the false-match probability to be $\lesssim 1\%$. Sources with no secure spectroscopic redshift have these two columns set to "–1.000" and "–1", respectively. Note that there are also photometric redshifts available in the literature (e.g., Mobasher et al. 2004; Wolf et al. 2004), but these are not included in our catalogs.

14. Column 29: the corresponding ≈1 Ms CDF-S source number from the main *Chandra* catalog presented in A03 (see column 1 of Table A2a in A03). We matched our X-ray source positions to A03 source positions using a matching radius that is the quadratic sum of the $\approx 3\sigma$ positional errors of the CDF-S and A03 X-ray sources. The 3σ positional error of a CDF-S source is approximately twice the positional error quoted in column 4 (i.e., $2\Delta_x$), and that of an A03 source is approximately twice the positional error quoted in Table A2a of A03. The false match probability is less than 1% with this matching radius. Only one A03 match was found for each matched source. In one case where two close-double sources matched to one A03 source, we chose the source with the smallest offset (source "433") as the most-probable match. We manually set the counterpart of the source with source number "437" to be source "312" in A03, because A03 apparently underestimated the positional error of this source. Sources with no A03 match have a value of "–1".

15. Columns 30 and 31: the right ascension and declination of the corresponding A03 source indicated in column 29. Sources with no A03 match have right ascension and declination values set to "00 00 00.00" and "–00 00 00.0".

16. Columns 32 and 33: the corresponding ≈1 Ms CDF-S source "ID" number and "XID" number from the main *Chandra* catalog presented in G02. When matching our CDF-S source positions with G02 counterparts, we removed offsets to the G02 positions of $-1\farcs2$ in right ascension and $+0\farcs8$ in declination (see §A3 of A03); these positions are corrected in the quoted source positions in columns 34 and 35. We used a matching radius that is the quadratic sum of the $\approx 3\sigma$ positional errors of the CDF-S and G02 X-ray sources. The 3σ positional error of a CDF-S source is approximately twice the positional error quoted in column 4, and that of a G02 source is quoted in Table 2 of G02. Only one G02 match was found for each matched source. In three cases where two close-double sources matched to one G02 source, we chose the source with the smallest offset (sources "142", "195" and "275") as the most-probable match. Sources with no G02 match have a value of "–1".

17. Columns 34 and 35: the right ascension and declination of the corresponding G02 source indicated in columns 32 and 33. Note that the quoted positions have been corrected by the offsets described in columns 32 and 33 (see §A3 of A03). Sources with no G02 match have right ascension and declination values set to "00 00 00.00" and "–00 00 00.0".

18. Columns 36–38: the effective exposure times determined from the standard-band exposure maps (see §3.1 for details on the exposure maps). Dividing the counts listed in columns 6–14 by the corresponding effective exposures will provide vignetting-corrected and quantum-efficiency degradation corrected count rates.

19. Columns 39–41: the band ratio, defined as the ratio of counts between the hard and soft bands, and the corresponding upper and lower errors, respectively. Quoted band ratios have been corrected for differential vignetting between the hard band and soft band using the appropriate exposure maps. Errors for this quantity are calculated following the "numerical method" described in §1.7.3 of Lyons (1991); this avoids the failure of the standard approximate variance formula when the number of counts is small (see §2.4.5 of Eadie et al. 1971). Note that the error distribution is not Gaussian when the number of counts is small. Upper limits are calculated for sources detected in the soft band but not the hard band, and lower limits are calculated for sources detected in the hard band but not the soft band. For these sources, the upper and lower errors are set to the computed band ratio. Sources detected only in the full band have band ratios and corresponding errors set to "–1.00".

20. Columns 42–44: the effective photon index (Γ) with upper and lower errors, respectively, for a power-law model with the Galactic column density given in §1. When the number of source counts is not low, the effective photon index has been calculated based on the band ratio in column 39 using the CXC's Portable, Interactive, Multi-Mission Simulator (PIMMS). Upper limits are calculated for sources detected in the hard band but not the soft band, and lower limits are calculated for sources detected in the soft band but not the hard band. For sources with only limits on the effective photon index, the upper and lower errors are set to the computed effective photon index.

    A source with a low number of counts is defined as being (1) detected in the soft band with < 30 counts and not detected in the hard band, (2) detected in the hard band with < 15 counts and not detected in the soft band, (3) detected in both the soft and hard bands, but with < 15 counts in each, or (4) detected only in the full band. When the number of counts is low, the photon index is poorly constrained and is set to $\Gamma = 1.4$, a representative value for faint sources that should yield reasonable fluxes. In this case, the upper and lower errors are set to "0.00".

21. Columns 45–47: observed-frame fluxes in the three standard bands; quoted fluxes are in units of ergs cm^{-2} s^{-1}. Fluxes have been computed using the counts in columns 6–14, the appropriate exposure maps (columns 36–38), and the effective photon indices

given in column 42. The fluxes have not been corrected for absorption by the Galaxy or material intrinsic to the source. For a power-law model with $\Gamma = 1.4$, the soft-band and hard-band Galactic absorption corrections are ≈2.1% and ≈ 0.1%, respectively. More accurate fluxes for these sources would require direct fitting of the X-ray spectra for each observation, which is model dependent and beyond the scope of this paper.

22. Column 48: the logarithm of the minimum false-positive probability run with WAVDETECT in which each source was detected (see §3.2). A lower false-positive probability indicates a more significant source detection. 398 (≈ 86%) and 357 (≈ 77%) of our sources are detected with false-positive probability thresholds of 1×10^{-7} and 1×10^{-8}, respectively.

23. Column 49: notes on the sources. "E" refers to sources at the edge that lie partially outside of the survey area. "S" refers to close doubles or triples where manual separation was required. "B" refers to sources with background counts estimated using the background maps (see columns 6–14 of Table 2).

In Table 3 we summarize the source detections in the three standard bands. In total 462 point sources are detected, 327 of which were present in the main *Chandra* catalogs for the ≈1 Ms CDF-S (G02 and A03), and thus 135 sources are new. For the 308 sources that were detected in the main catalog of A03, we find general agreement between the derived X-ray properties presented here and in A03. For example, we have compared the full-band count rates of these 308 sources between the two catalogs. The median ratio of the count rates is ≈ 0.98 with an interquartile range of ≈0.85–0.12. Furthermore, the approximately doubled exposure improves the source positions and spectral constraints significantly, and thus the ≈2 Ms CDF-S catalogs presented here supersede those in A03.

Eighteen of the 326 sources detected in the main catalog of A03 are undetected here. Nine of these were detected in WAVDETECT runs with a false-positive probability threshold of 1×10^{-5} in the present analysis. The other nine sources were weakly detected in A03 with less than 17 full-band counts. We examined the regions of these nine sources in the three ≈ 2 Ms images and found no emission clearly distinct from the background. Ten of the eighteen sources have optical counterparts in the WFI *R*-band source catalog within 1.″3, and three of them are present in the supplementary optically bright *Chandra* catalog (see §3.3.3), suggesting that they are likely true X-ray sources. As the second ≈ 1 Ms exposure was taken ≈ 7 years later, these eighteen sources could be below our detection limit due to source variability or background fluctuations. A 30% median flux variability has been observed for sources in the first ≈ 1 Ms data set (Paolillo et al. 2004), which is expected to increase here owning to the long observation interval. There is also the possibility that some of the missing sources were false detections in A03, since ≈3–9 false detections were expected (A03).

Four of the 304 sources in the main catalog of G02 are not detected here, two of which were detected in WAVDETECT runs with a false-positive probability threshold of 1×10^{-5}. All four sources lie at large off-axis angles, and none of them is in the A03 main catalog. These sources could be below our detection limit due to source variability or background fluctuations. Note that 19 G02 sources that were not detected in A03 are detected here, suggesting that these are likely true sources. These sources were probably not reported in the A03 main catalog due to the conservative WAVDETECT false-positive probability threshold (1×10^{-7}) adopted in that work.

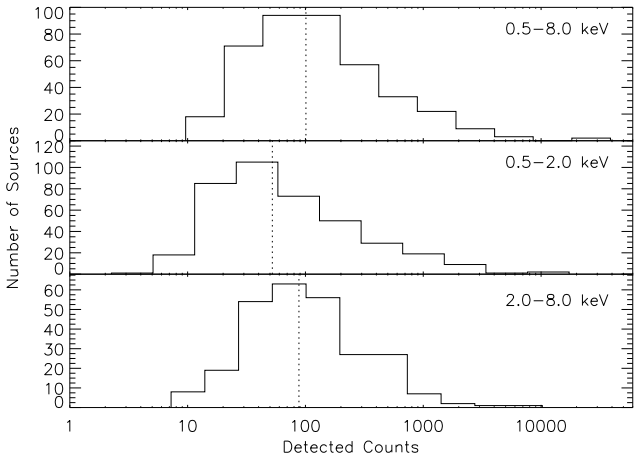

FIG. 7.— Histograms showing the distributions of detected source counts for sources in the main *Chandra* catalog in the full (*top*), soft (*middle*), and hard (*bottom*) bands. Sources with upper limits have not been included in these diagrams. The vertical dotted lines indicate median numbers of counts in each band (see Table 3).

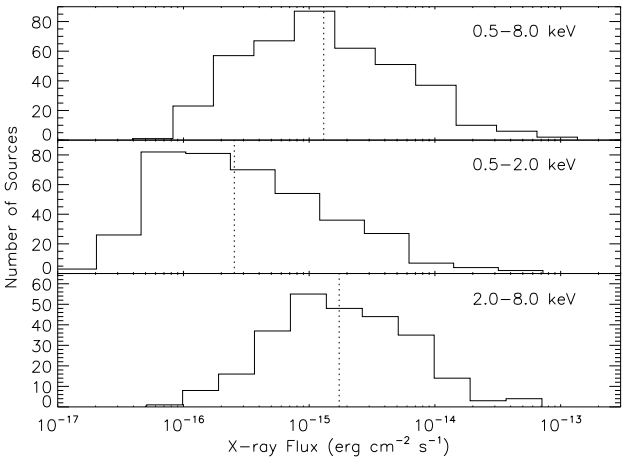

FIG. 8.— Histograms showing the distributions of X-ray fluxes for sources in the main *Chandra* catalog in the full (*top*), soft (*middle*), and hard (*bottom*) bands. Sources with upper limits have not been included in this figure. The vertical dotted lines indicate the median fluxes of 1.3×10^{-15}, 2.5×10^{-16} and 1.7×10^{-15} ergs cm^{-2} s^{-1} for the full, soft, and hard bands, respectively.

In Table 4 we summarize the number of sources detected in one band but not another. There are three sources detected only in the hard band. For comparison, there is one source in the ≈ 1 Ms CDF-S that was detected only in the hard band (A03). In Figure 7 we show the distributions of detected counts in the three standard bands. The median numbers of counts for the full band, soft band and hard band are ≈ 101, ≈ 53 and ≈ 89, respectively. There are 202 sources with > 100 full-band counts, for which basic spectral analyses are possible, and 33 sources with > 1000 full-band counts. In Figure 8 we show the distributions of X-ray flux in the three standard bands. The X-ray fluxes in this survey span roughly four orders of magnitude, with ≈50% of the sources having soft-band and hard-band fluxes of less than 2.5×10^{-16} ergs cm^{-2} s^{-1} and 1.7×10^{-15} ergs cm^{-2} s^{-1}, respectively.

In Figure 9 we show "postage-stamp" images from the

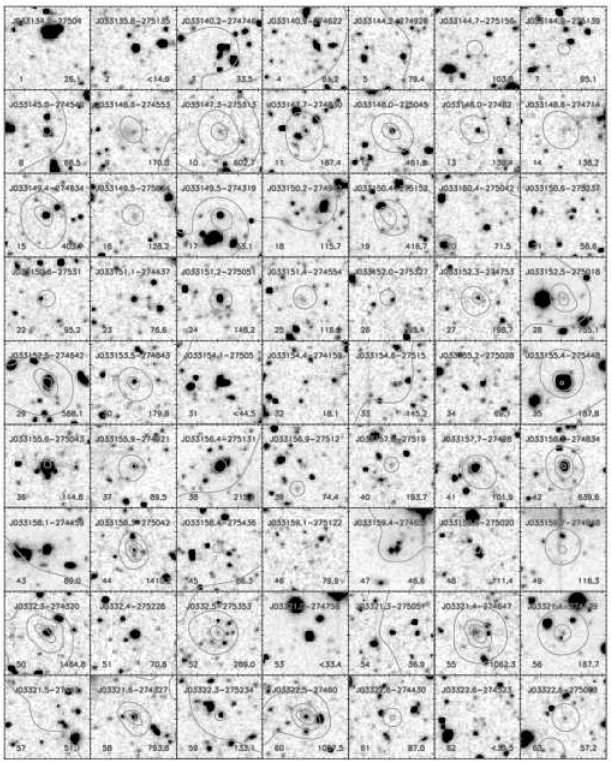

FIG. 9.— WFI *R*-band postage-stamp images for the sources in the main *Chandra* catalog with full-band adaptively smoothed X-ray contours overlaid. The contours are logarithmic in scale and range from ≈0.003%–30% of the maximum pixel value. The label at the top of each image gives the source name, which is composed of the source coordinates, while numbers at the bottom left and right-hand corners correspond to the source number (see column 1 of Table 2) and the full-band counts or upper limits (with a "<" sign) on the full-band counts, respectively. In several cases no X-ray contours are present, either because these sources were not detected in the full band or the full-band counts are low and CSMOOTH has suppressed the observable emission in the adaptively smoothed images. Each image is 25″ on a side, and the source of interest is always located at the center of the image. Only one of the 8 pages of cutouts is included here; all 8 pages are available in the electronic edition.

WFI *R*-band image with adaptively smoothed full-band contours overlaid for sources in the main *Chandra* catalog. The wide range of X-ray source sizes observed in these images is largely due to PSF broadening with off-axis angle. Figure 10*a* shows the positions of sources detected in the main *Chandra* catalog. The source density is highest close to the average aim point where the sensitivity is highest. Different symbol sizes represent different significances of source detection with WAVDETECT (see column 48 of Table 2). New X-ray sources that are not present in the G02 or A03 main catalogs are indicated as filled circles; 135 new sources are detected, of which 15 lie outside the solid-angle coverage of the first ≈ 1 Ms exposure.

Figure 11 shows the band ratio as a function of full-band count rate for sources in the main *Chandra* catalog. We also derived average band ratios by stacking the individual sources together using a procedure similar to that of Lehmer et al. (2008). The average band ratio rises at lower count rates. The corresponding average photon index flattens from $\Gamma \approx 1.8$ to $\Gamma \approx 0.8$ for full-band count rates of $\approx 10^{-2}$ to $\approx 2 \times 10^{-4}$ counts s^{-1}. This trend has been reported in other studies (e.g., Tozzi et al. 2001; A03; L05) and is due to an increase in the number of absorbed AGNs detected at fainter fluxes. The average photon index does not continue getting flatter below full-band count rates of $\approx 2 \times 10^{-4}$ counts s^{-1}, probably due to the increased contribution from normal and starburst galaxies at these lowest count rates (Bauer et al. 2004). In Figure 12*a* we show the WFI *R*-band magnitude versus soft-band flux for X-ray sources in the main catalog, as well as the approximate flux ratios for AGNs and galaxies (e.g., Maccacaro et al. 1988; Stocke et al. 1991; Hornschemeier et al. 2001; Bauer et al. 2004). More than half (304) of the X-ray sources lie in the region expected for AGNs, 74 of which are new sources. A significant minority (158) of the sources lie in the region for normal and starburst galaxies, 61 of which are new sources. The new sources have an increased fraction of normal and starburst galaxies. This source characterization, based only on the X-ray–to–optical flux ratio, is only approximate and will be refined in future studies.

3.3.2. *Supplementary CDF-S plus E-CDF-S Chandra Source Catalog*

We can gain additional sensitivity in the outer portions of the ≈ 2 Ms CDF-S footprint by including the ≈ 250 ks E-CDF-S (L05) observations. To this end, we processed and registered the E-CDF-S exposures in the same manner as our CDF-S observations. Notably, because of the different coverage of the CDF-S and E-CDF-S (see Figure 2 of L05), the PSF sizes for the E-CDF-S near the average aim point for the CDF-S are substantially larger than those for the CDF-S. The E-CDF-S will likely only contribute additional background for all but the strongest sources around the center of the field. Thus, we excluded the E-CDF-S event lists within 4′ of the CDF-S average aim point. We also masked out portions of the E-CDF-S where the CDF-S exposure time was zero. Images and exposure maps were cropped in a similar manner.

We ran WAVDETECT with a false-positive probability threshold of 1×10^{-6} on the three standard-band images for the combined CDF-S plus E-CDF-S, detecting 86 sources not present in the main *Chandra* source catalog. The positions of these sources have been improved following the procedure described in §3.3.1. Due to the drastically different overlapping PSFs, the derived properties of these X-ray sources are not as reliable as those in the main catalog. Therefore we present these sources in Table 5 as a supplementary CDF-S plus E-CDF-S *Chandra* source catalog. For sources already detected in the E-CDF-S (L05), we took the photometry data from L05 directly. For new sources, photon counts and effective exposure times were extracted separately from the CDF-S and E-CDF-S data sets and then summed to give a total number of counts and a total effective exposure time. The format of Table 5 is very similar to that of Table 2, with a few details given below.

1. Columns 1–28: the format of these columns is exactly the same as that of columns 1–28 in Table 2, so the column descriptions in §3.3.1 are applicable. Note that for sources detected in the E-CDF-S (see column 29 or 52), the source counts and their uncertainties were taken from L05 directly.

2. Column 29: the corresponding ≈250 ks E-CDF-S source number from the main *Chandra* catalog presented in L05 (see column 1 of Table 2 in L05). We matched our X-ray source positions to L05 source positions using a matching radius that is the quadratic

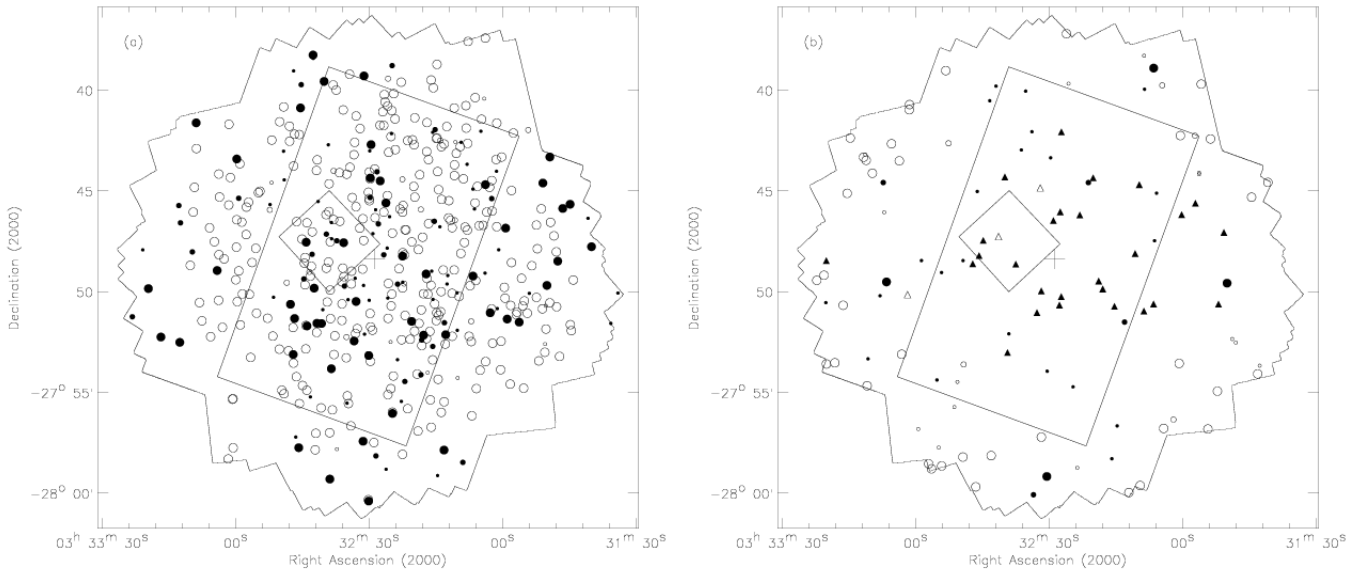

FIG. 10.— Positions of the sources in (*a*) the main *Chandra* catalog and (*b*) the supplementary *Chandra* catalogs. Circles represent X-ray sources in (*a*) the main *Chandra* catalog and (*b*) the supplementary CDF-S plus E-CDF-S *Chandra* catalog. Open circles represent X-ray sources that were previously detected in (*a*) the main catalogs of G02 or A03 and (*b*) the main catalogs of G02, A03, or L05. Filled circles represent new sources. Sizes indicate the maximum detection significance corresponding to WAVDETECT false-positive probability detection thresholds of 1×10^{-8} (*large circles*), 1×10^{-7} (*medium circles*), and 1×10^{-6} (*small circles*). Sources in the optically bright catalog are shown as open triangles (previously detected in the main catalog of A03) and filled triangles (new sources) in (*b*). For sources in the CDF-S plus E-CDF-S catalog, their detection significances are preferentially higher near the edge of the field due to the contribution of the E-CDF-S exposure. The regions and the cross symbol have the same meaning as those in Fig. 1.

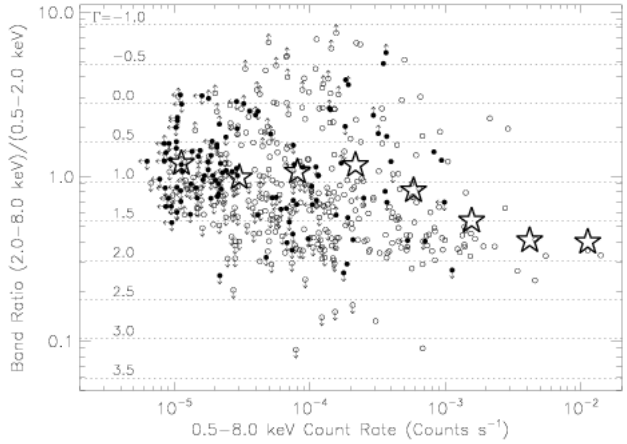

FIG. 11.— Band ratio vs. full-band count rate for sources in the main *Chandra* catalog. Open circles represent X-ray sources that were detected in the main catalogs of G02 or A03. Filled circles represent new sources. Plain arrows indicate upper or lower limits. Sources detected only in the full band cannot be plotted. The open stars show average band ratios as a function of full-band count rate derived from stacking analyses. Horizontal dotted lines show the band ratios corresponding to given effective photon indices; these were calculated using PIMMS.

sum of the $\approx 3\sigma$ positional errors of the CDF-S and L05 X-ray sources. The 3σ positional error of a CDF-S source is approximately twice the positional error quoted in column 4, and that of an L05 source is approximately twice the positional error quoted in Table 2 of L05. Only one L05 match was found for each matched source. Sources with no L05 match have a value of "–1".

3. Columns 30 and 31: the right ascension and declination of the corresponding L05 source indicated in column 29. Sources with no L05 match have right ascension and declination values set to "00 00 00.00" and "–00 00 00.0".

4. Columns 32–51: the format of these columns is exactly the same as that of columns 29–48 in Table 2, so the column descriptions in §3.3.1 are applicable. Note that for sources detected in the E-CDF-S (see column 29 or 52), the source exposure times, band ratios, photon indices, and fluxes were taken from L05 directly.

5. Column 52: notes on the sources. "L" refers to sources that were detected in the ≈250 ks E-CDF-S (L05).

The 86 CDF-S plus E-CDF-S sources have effective exposures up to ≈ 1.9 Ms. Their positional uncertainties were estimated following equation (1), though the positional accuracy of the off-axis sources will often have been improved due to the small PSF sizes of the E-CDF-S. 60 ($\approx 70\%$) of the sources have optical counterparts. Two of the 86 sources have counterparts in the A03 main catalog and another two have counterparts in the G02 main catalog. In addition, 53 of the sources were detected in the main catalog of L05. There are thus 30 new sources in this supplementary catalog. 50 ($\approx 57\%$) and 41 ($\approx 47\%$) of these sources are detected with false-positive probability thresholds of 1×10^{-7} and 1×10^{-8}, respectively.

Figure 10*b* shows the positions of sources detected in the supplementary CDF-S plus E-CDF-S catalog. Different symbol sizes represent different significances of the source detection with WAVDETECT (see column 51 of Table 5).

3.3.3. *Supplementary Optically Bright Chandra Source Catalog*

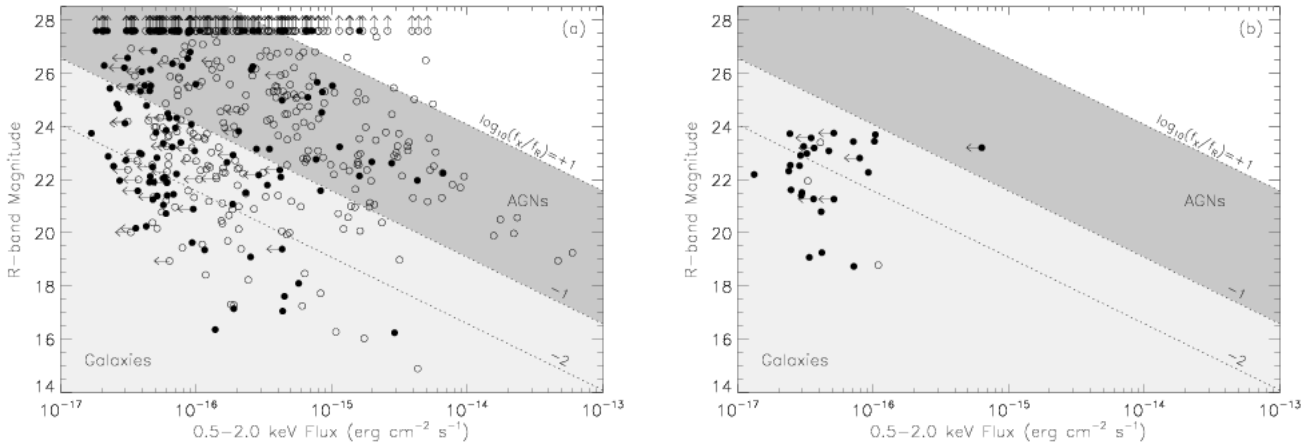

FIG. 12.— WFI *R*-band magnitude vs. soft-band flux for X-ray sources in (*a*) the main catalog and (*b*) the supplementary optically bright catalog. Open circles represent X-ray sources that were detected in the main catalogs of G02 or A03. Filled circles represent new sources. Sources without an optical counterpart are plotted as upward arrows. Diagonal lines indicate constant flux ratios. The shaded areas show the approximate flux ratios for AGNs (dark gray) and galaxies (light gray).

Since the density of optically bright sources on the sky is comparatively low, we constructed a supplementary *Chandra* source catalog including X-ray sources detected at a lower X-ray significance threshold than that used in the main catalog and having bright optical counterparts. We ran WAVDETECT with a false-positive probability threshold of 1×10^{-5} on the three CDF-S images, and we found 132 lower significance X-ray sources not present in the main *Chandra* source catalog or the supplementary CDF-S plus E-CDF-S catalog.

Bright optical sources were selected from the WFI *R*-band source catalog described in §3.1, with an *R*-band magnitude brighter than 23.8. This *R*-band cutoff was empirically determined to provide a good balance between the number of detected sources and the expected number of false sources. We searched for bright optical counterparts to the low-significance X-ray sources using a matching radius of $1\farcs3$. A matching radius of $1\farcs3$ was chosen as a compromise between having too few matches and too many false matches. In total 30 optically bright X-ray sources were found. We estimated the expected number of false matches by manually shifting the X-ray source coordinates in right ascension and declination by $5\farcs0$ and $10''$ (both positive and negative shifts) and recorrelating with the optical sources. On average, the number of false matches is ≈ 3 ($\approx 10\%$), demonstrating that the majority of the 30 X-ray matches are real X-ray sources.

The supplementary optically bright *Chandra* source catalog is presented in Table 6. These sources typically have 4–35 counts in the band in which they were detected. The format of Table 6 is similar to that of Table 2, with the details of the columns given below.

1. Column 1: the source number. Sources are listed in order of increasing right ascension.

2. Columns 2 and 3: the right ascension and declination of the X-ray source, respectively. The WAVDETECT positions are used here for these faint X-ray sources. Whenever possible, we have quoted the position determined in the full band; when a source is not detected in the full band, we used, in order of priority, the soft-band position or hard-band position.

3. Column 4: the positional uncertainty. For these faint X-ray sources, the positional uncertainty is set to $1\farcs2$, the approximate 90th percentile of the optical–X-ray positional offsets given in column 17.

4. Column 5: the off-axis angle of the X-ray source in arcminutes (see column 5 of Table 2 for details).

5. Columns 6–14: the source counts and the corresponding 1σ statistical errors (Gehrels 1986) or the upper limits on source counts for the three standard bands, respectively. When a source is detected in a given band, the photometry is taken directly from WAVDETECT. When a source is not detected, an upper limit is calculated (see columns 6–14 of Table 2 for details).

6. Columns 15 and 16: the right ascension and declination of the optical counterpart.

7. Column 17: the measured offset between the optical and X-ray sources in arcseconds.

8. Column 18: the *R*-band AB magnitude of the optical counterpart.

9. Columns 19–26: the *i*, *z*, and K_s band AB magnitudes and the IRAC 5.8 μm flux density of the optical counterpart, and the correspoding source ID in the optical and infrared catalogs (see columns 19–26 of Table 2 for details).

10. Columns 27 and 28: the corresponding spectroscopic redshift and the reference for the redshift (see columns 27 and 28 of Table 2 for details).

11. Column 29: the corresponding $\approx$1 Ms CDF-S source number from the main *Chandra* catalog presented in A03 (see column 1 of Table 3a in A03). We used a matching radius that is the quadratic sum of the $\approx 3\sigma$ positional errors of the CDF-S and A03 X-ray sources. The 3σ positional error of a CDF-S source is $\approx 1\farcs3$, and that of an A03 source is approximately twice the positional error quoted in Table A2a of A03. Only one A03 match was found for each matched source. Supplementary sources with no A03 match have a value of "–1". There are no matches to the main source catalog in G02, so we do not list the match results in this table.

12. Columns 30 and 31: the right ascension and declination of the corresponding A03 source indicated in column 29. Sources with no A03 match have right ascension and declination values set to "00 00 00.00" and "–00 00 00.0".

13. Columns 32–34: the effective exposure times derived from the standard-band exposure maps.

14. Column 35: the photon index used to calculate source fluxes (columns 36–38). We used a constant photon index of $\Gamma = 2.0$ since our source-selection technique preferentially selects objects with flux-ratios $f_{0.5\text{–}2.0\ \mathrm{keV}}/f_R < 0.1$, which are observed to have effective photon indices of $\Gamma \approx 2$ (e.g., § 4.1.1 of Bauer et al. 2004).

15. Column 36–38: observed-frame fluxes in the three standard bands; quoted fluxes are in units of ergs cm^{-2} s^{-1} and have been calculated assuming $\Gamma = 2.0$. The fluxes have not been corrected for absorption by the Galaxy or material intrinsic to the sources (see columns 45–47 of Table 2 for details).

The WFI *R*-band magnitudes of these supplementary sources span R =18.7–23.8. In Figure 12*b* we show the *R*-band magnitude versus soft-band flux for the 30 optically bright X-ray sources. The approximate flux ratios for AGNs and galaxies are also plotted. The majority of the sources have the X-ray–to–optical flux ratios expected for normal and starburst galaxies. Some of these sources may be low-luminosity AGNs; only one source is detected in the hard band, suggesting that they are unlikely to be luminous absorbed AGNs. Note that the supplementary optically bright sources are not representative of the faintest X-ray sources as a whole, because our selection criteria preferentially select optically bright and X-ray faint non-AGNs (e.g., A03; Hornschemeier et al. 2003). The positions of the sources in the supplementary optically bright catalog are shown in Figure 10*b*.

4. BACKGROUND AND SENSITIVITY ANALYSIS

Background maps were created for the three standard bands. We first masked out the point sources from the main *Chandra* catalog using apertures with radii twice that of the ≈90% PSF encircled-energy radii; approximately 12% of the pixels were masked out. The resultant images should include minimum contributions from detected point sources. However, they will include contributions from a few extended sources (e.g., Bauer et al. 2002), which will cause a slight overestimation of the measured background. Even with a $\approx$ 2 Ms exposure, about 79% of the pixels have no background counts in the full band. For such a small number of detected counts per pixel, the expected counts distribution is Poissonian. We compared the background-count distributions to Poisson distributions with the mean number of background counts per pixel using the Kolmogorov-Smirnov test, and we found them to be very similar in all three standard bands for various regions across the survey field (see §4.2 of A03 for more details on the tests). We filled in the masked regions for each source with a local background estimate by constructing a probability distribution of counts using an annulus with inner and outer radii of 2 and 4 times the ≈90% PSF encircled-energy radius, respectively. The background properties are summarized in Table 7. The total background includes contributions from the unresolved cosmic background, particle background, and instrumental background (e.g., Markevitch 2001; Markevitch et al. 2003). For our analyses we are only interested in the total background and do not distinguish between these different components. The mean background count rates are ≈ 20%–30% higher compared to the $\approx$ 2 Ms CDF-N (A03) or the $\approx$ 250 ks E-CDF-S (L05), which are reasonable variations given the variability of the particle and instrumental background components over the past several years.

The faintest sources in the main *Chandra* catalog have ≈ 5 counts in the soft band and ≈ 8 counts in the hard band (see Table 3). For a $\Gamma = 1.4$ power law with Galactic absorption, the corresponding soft-band and hard-band fluxes at the average aim point are $\approx 1.6 \times 10^{-17}$ ergs cm^{-2} s^{-1} and $\approx 9.0 \times 10^{-17}$ ergs cm^{-2} s^{-1}, respectively. This provides an estimate of the ultimate sensitivity of this survey. However, these numbers are only relevant for a small area close to the average aim point. To determine the sensitivity across the field it is necessary to take into account the broadening of the PSF with off-axis angle, as well as changes in the effective exposure and background rate across the field. Following L05, we estimated the sensitivity across the field by employing a Poisson model, The resulting relation can be approximately represented by

$$\log N = \alpha + \beta \log b + \gamma (\log b)^2 + \delta (\log b)^3 \qquad (2)$$

where N is the required number of counts for detection, and b is the number of background counts in a source cell; α = 0.917, β = 0.414, γ = 0.0822, and δ = 0.0051 are fitting constants. For the sensitivity calculations here, we measured the number of background counts b in the background maps using an aperture size of 70% of the PSF encircled-energy radius. The 70% encircled-energy radius was chosen as a compromise between having too few source counts and too many background counts.

Following equation (2), we constructed sensitivity maps using the background and exposure maps, assuming a $\Gamma = 1.4$ power-law model with Galactic absorption. Since we do not filter out detected sources with our sensitivity maps, a small fraction of sources have fluxes slightly below these sensitivity limits (4 sources in the full band, 14 sources in the soft band, and 7 sources in the hard band). The full-band sensitivity map is shown in Figure 13, and in Figure 14 we show plots of solid angle versus flux limit for the full, soft, and hard bands. The $\approx$1 arcmin^2 region at the average aim point has soft-band and hard-band sensitivity limits of $\approx 1.9 \times 10^{-17}$ ergs cm^{-2} s^{-1} and $\approx 1.3 \times 10^{-16}$ ergs cm^{-2} s^{-1}, respectively. Solid angles for the $\approx$ 2 Ms CDF-N have been plotted for comparison in Figure 14 (dotted curves), which appear to be similar to those for the CDF-S.[28]

5. NUMBER COUNTS FOR THE MAIN *CHANDRA* CATALOG

Cumulative number counts, $N(>S)$, for the soft and hard bands were calculated for the $\approx$ 2 Ms CDF-S. To quantify the effects of incompleteness and bias, we took a similar approach to the one in Bauer et al. (2004) and created 200 Monte Carlo simulated observations in both the soft and hard bands. We added simulated sources at random positions to the

[28] The CDF-N sensitivity limits were calculated following the same method described above.

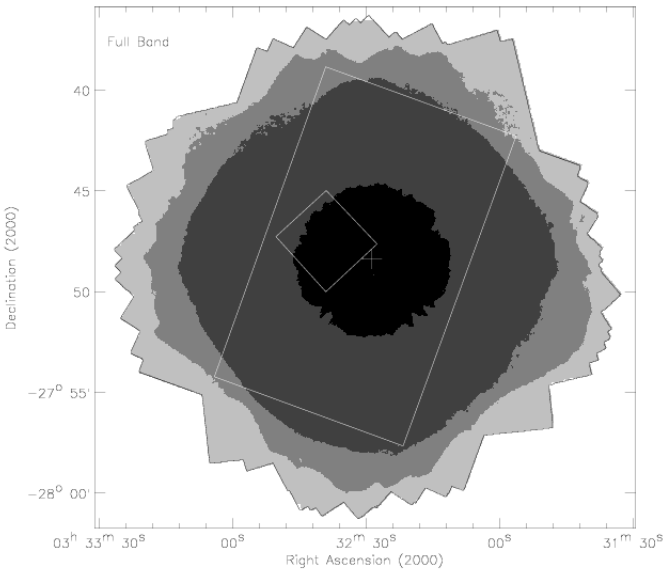

FIG. 13.— Full-band sensitivity map of the 2 Ms CDF-S. This sensitivity map has been created following §4. The gray-scale levels (from black to light gray) represent areas with flux limits (in units of ergs cm^{-2} s^{-1}) of $< 10^{-16}$, 10^{-16}–3.3×10^{-16}, 3.3×10^{-16}–10^{-15}, and $> 10^{-15}$, respectively. The regions and the cross symbol have the same meaning as those in Fig. 1.

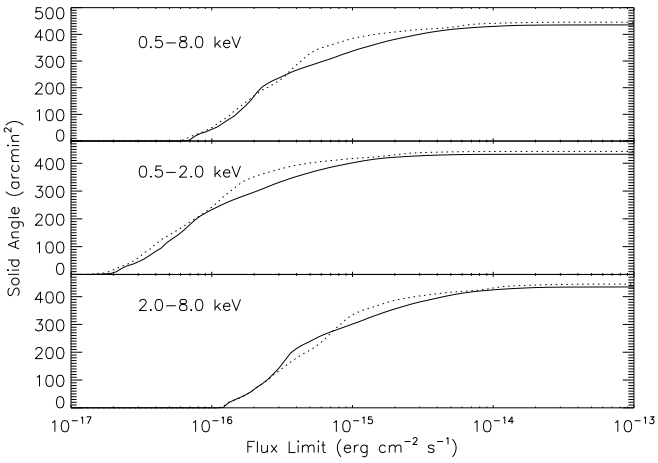

FIG. 14.— Survey solid angle as a function of the flux limit for the full (*top*), soft (*middle*), and hard (*bottom*) bands, determined following §4. Data are plotted as solid curves for the ≈ 2 Ms CDF-S, and as dotted curves for the ≈ 2 Ms CDF-N. The flux limits at the average aim point of the CDF-S are $\approx 7.1\times10^{-17}$ ergs cm^{-2} s^{-1} (full band), $\approx 1.9\times10^{-17}$ ergs cm^{-2} s^{-1} (soft band), and $\approx 1.3\times10^{-16}$ ergs cm^{-2} s^{-1} (hard band).

background maps described in §4. The fluxes of these simulated sources were drawn randomly from the total number-count models of Moretti et al. (2003) between 1.6×10^{-17} and 10^{-11} ergs cm^{-2} s^{-1} in the soft band and 9×10^{-17} and 10^{-11} ergs cm^{-2} s^{-1} in the hard band. These fluxes were converted to X-ray photon counts using the exposure maps and a photon index of $\Gamma = 1.4$. Statistical errors were added to the counts to account for the effect of Eddington bias. Finally, counts for each simulated source were added to the background map following a PSF probability distribution function derived from the combined model PSF of the nearest real X-ray source in the main catalog. These model PSFs were produced using AE.

Source searching and photometry were performed on the simulated images using the same method as that used to produce the main catalog. A completeness correction factor (F) was estimated by comparing the number of simulated input sources with the number of simulated detected sources as a function of detected counts. A flux recovery correction factor (R) was calculated by comparing the simulated input counts with simulated measured counts. The correction factors are position- and count-dependent. For each of the 462 X-ray sources in the main catalog, we determined the two correction factors based on a sample of simulated sources within $2'$ of the source position and having similar exposure times. Sources close to the edge of the survey field are not well sampled, and thus we calculated cumulative number counts using only the 428 X-ray sources that are located within $10'$ of the average aim point. The completeness and flux recovery corrections remain close to unity above ∼50–100 counts. Below this point, *Chandra*'s varying PSF size and spatially dependent vignetting begin to affect source detection and photometry.

We set our minimum flux levels to 3×10^{-17} ergs cm^{-2} s^{-1} in the soft band and 2.5×10^{-16} ergs cm^{-2} s^{-1} in the hard band. These limits were chosen since at lower fluxes there are less than 10–15 additional sources contributing to the number counts, and thus the number counts at fainter levels have large uncertainties. The cumulative number of sources, $N(>S)$, brighter than a given flux, S, weighted by the appropriate aerial coverage, is

$$N(>S) = \sum_{S_i>S} (F_i\Omega_i)^{-1} \ , \qquad (3)$$

where Ω_i is the maximum solid angle for which a source with flux, S_i, could be detected. Each flux S has been corrected for flux bias assuming

$$S_i = R_i S_i^0 \ , \qquad (4)$$

where S_i^0 is the original flux quoted in the main catalog. The maximum solid angles were computed using the inner $10'$ radius regions of the sensitivity maps. We have also calculated 1σ errors for the cumulative distributions following Gehrels (1986).

Figure 15 displays the cumulative number counts and the corresponding 1σ errors for the main *Chandra* catalog. Cumulative number counts for several other surveys have also been shown for comparison. The derived ≈2 Ms CDF-S cumulative number counts are in general agreement with previous survey results for the ≈1 Ms CDF-S (Rosati et al. 2002) and the ≈250 ks E-CDF-S (L05), at around the 1σ confidence level over the entire flux range in the soft and hard bands. The apparent deviation between the ≈2 Ms and ≈1 Ms CDF-S soft-band number counts mainly comes from the difference in the count-rate–to–flux conversion factor used in these two surveys.[29] The *XMM-Newton* observations in the COSMOS field (Cappelluti et al. 2007) provide similar number counts, though not as deep as the CDF-S observations.

To make a consistent comparison with the ≈2 Ms CDF-N number counts, we analyzed the CDF-N observations in the

[29] An average photon index of $\Gamma = 1.4$ was used to calculate fluxes in Rosati et al. (2002), while in this survey, the photon index was estimated for each source separately and so was the count-rate–to–flux conversion factor (see §3.3.1). We did a test by calculating the soft-band fluxes using the conversion factor given by Rosati et al. (2002). The derived fluxes are ∼ 90% of those presented in the main catalog, and the resulting soft-band number counts are consistent with those for the ≈1 Ms CDF-S to within 1σ.

same way as in this paper. A main catalog of 575 X-ray sources was constructed. Number counts were calculated using the 496 X-ray sources located within 10′ of the average aim point, and these have been corrected for incompleteness and flux bias based on simulations. The CDF-N cumulative number counts are presented in Figure 15 (dotted curves), along with the ratios of the CDF-S to CDF-N number counts. In the soft band, the ≈2 Ms CDF-S number counts appear to be consistent with those for the ≈2 Ms CDF-N to within $\approx 1\sigma$ at fluxes above $\approx 2\times10^{-16}$ ergs cm^{-2} s^{-1}. Small differences (up to $\approx 3\sigma$) exist at fainter fluxes. In the hard band, the CDF-N number counts deviate above the 1σ errors of the CDF-S number counts at fluxes below $\approx 2\times10^{-15}$ ergs cm^{-2} s^{-1}; the difference at the faintest fluxes is ≈25% ($\approx 3\sigma$). Similar findings of differences between the CDF-N and CDF-S number counts have been reported in previous studies (e.g., Cowie et al. 2002; Moretti et al. 2003; Bauer et al. 2004), and it appears that this results from small field-to-field variations. Such field-to-field variations are generally believed to arise from the large-scale structure underlying the cosmic X-ray source distribution (e.g., Gilli et al. 2003; Yang et al. 2003).

6. SUMMARY

We have presented catalogs and basic analyses of X-ray point sources detected in the ≈ 2 Ms CDF-S, which is one of the two deepest *Chandra* surveys. The key points from this work are the following:

1. The entire CDF-S consists of 23 separate observations with 1.911 Ms of combined exposure. The survey covers an area of 435.6 arcmin^2.

2. The main *Chandra* source catalog consists of 462 sources that were detected using WAVDETECT with a false-positive probability threshold of 1×10^{-6}. These sources were detected in up to three X-ray bands: 0.5–8.0 keV, 0.5–2.0 keV, and 2–8 keV; 135 of these sources are new.

3. The first supplementary *Chandra* source catalog contains 86 sources that were generated by merging the ≈ 250 ks E-CDF-S with the CDF-S, which provides additional sensitivity in the outer regions of the CDF-S.

4. The second supplementary *Chandra* source catalog contains 30 sources that were detected at a lower X-ray significance threshold of 1×10^{-5} and that have bright optical counterparts ($R < 23.8$).

5. Source positions for the main and supplementary CDF-S plus E-CDF-S *Chandra* catalogs have been determined using centroid and matched-filter techniques; the median positional uncertainty is $\approx 0.''36$.

6. The basic X-ray and optical properties of the point sources indicate a variety of source types. More than half of the sources in the main *Chandra* catalogs appear to be AGNs. Of the 135 newly detected sources, ≈55% appear to be AGNs while ≈45% appear to be starburst and normal galaxies. The majority of the sources in the supplementary optically bright catalog are expected to be normal and starburst galaxies.

7. The average backgrounds in the 0.5–2.0 and 2–8 keV bands are 0.066 and 0.167 counts Ms^{-1} pixel^{-1}, respectively. Thus these observations are nearly photon limited near the aim point and could be extended to substantially greater depths with further exposure. The background count distributions are very close to Poisson distributions. The on-axis flux limits in the 0.5–2.0 keV and 2–8 keV bands are $\approx 1.9\times10^{-17}$ ergs cm^{-2} s^{-1} and $\approx 1.3\times10^{-16}$ ergs cm^{-2} s^{-1}, respectively.

8. Compared to the other deepest *Chandra* survey, the ≈ 2 Ms CDF-N, the CDF-S has similar effective exposure coverage and sensitivity limits. The cumulative number counts of these two fields are consistent with each other to within $\approx 1\,\sigma$ at fluxes above $\approx 2\times10^{-16}$ ergs cm^{-2} s^{-1} in the soft band. The CDF-N number counts are up to ≈ 25% higher than the CDF-S number counts at the faintest fluxes in the soft and hard bands, indicating small field-to-field variations.

7. ACKNOWLEDGEMENTS

Support for this work was provided by NASA through *Chandra* Award SP8-9003A (BL, FEB, WNB) issued by the *Chandra* X-ray Observatory Center, which is operated by the Smithsonian Astrophysical Observatory. We also acknowledge the financial support of the Royal Society (DMA and IRS), the Science and Technology Facilities Council fellowship program (BDL), NSF grant 06-7634 (DPS), contract ASI–INAF I/023/05/0 and grant PRIN-MIUR 2006-02-5203 (AC, RG, and CV). We thank H.D. Tananbaum for allocating the time for these observations and T. L. Aldcroft, P. Broos and L. K. Townsley for helpful discussions.

REFERENCES

Alexander, D. M., et al. 2003, AJ, 126, 539 (A03)
Baganoff, F. K., et al. 2003, ApJ, 591, 891
Bauer, F. E., Alexander, D. M., Brandt, W. N., Schneider, D. P., Treister, E., Hornschemeier, A. E., & Garmire, G. P. 2004, AJ, 128, 2048
Bauer, F. E., et al. 2002, AJ, 123, 1163
Beckwith, S. V. W., et al. 2006, AJ, 132, 1729
Bertin, E., & Arnouts, S. 1996, A&AS, 117, 393
Bickel, P. J. 1992, in Statistical Chanllenges in Modem Astronomy, ed, E. D. Feigelson & G. J. Babu (New York: Springer), 320
Boller, T., Bertoldi, F., Dennefeld, M., & Voges, W. 1998, A&AS, 129, 87
Brandt, W. N., & Hasinger, G. 2005, ARA&A, 43, 827
Brandt, W. N., et al. 2001, AJ, 122, 1
Broos, P., et al. 2000, User's Guide for the TARA Package (University Park: Pennsylvania Sate Univ.)
Caldwell, J. A. R., et al. 2008, ApJS, 174, 136
Cappelluti, N., et al. 2007, ApJS, 172, 341
Cowie, L. L., Garmire, G. P., Bautz, M. W., Barger, A. J., Brandt, W. N., & Hornschemeier, A. E. 2002, ApJ, 566, L5
Eadie, W. T., Dryard, D., James, F. E., Roos, M., & Sadoulet, B. 1971, Statistical Methods in Expermental Physics (Amsterdam: North-Holland)
Feigelson, E. D., Broos, P. S., & Gaffney, J. 2000, Memo on the Optimal Extraction Radius for ACIS Point Souces (University Park: Pennsylvania State Univ.)
Freeman, P. E., Kashyap, V., Rosner, R., & Lamb, D. Q. 2002, ApJS, 138, 185
Garmire, G. P., Bautz, M. W., Ford, P. G., Nousek, J. A., & Ricker, Jr., G. R. 2003, Proc. SPIE, 4851, 28
Gehrels, N. 1986, ApJ, 303, 336
Gendreau, K. C., et al. 1995, PASJ, 47, L5
Giacconi, R., et al. 2002, ApJS, 139, 369 (G02)
Giavalisco, M., et al. 2004, ApJ, 600, L93
Gilli, R., et al. 2003, ApJ, 592, 721

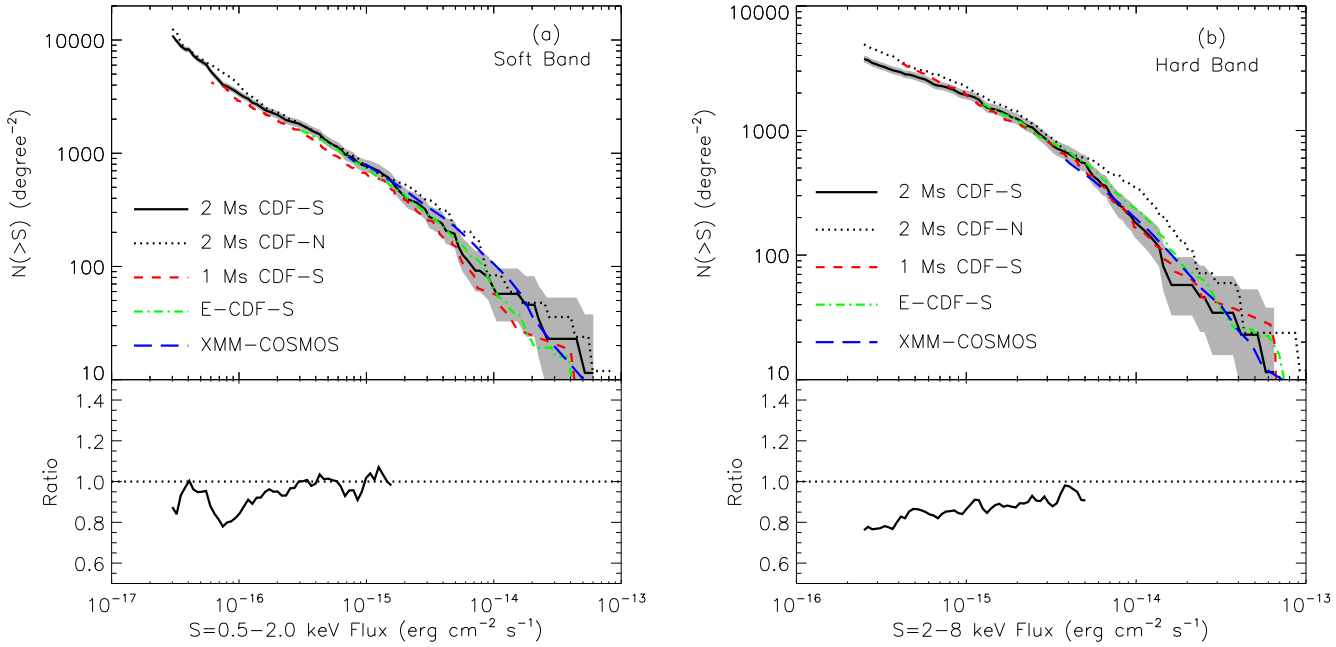

FIG. 15.— *Top*: Number of sources, $N(>S)$, brighter than a given flux, S, for the (*a*) soft band and (*b*) hard band. The ≈2 Ms CDF-S data are plotted as black solid curves with the 1σ errors plotted as gray shaded areas. The cumulative number counts were computed using 428 X-ray sources in the main *Chandra* catalog that are located within $10'$ of the average aim point, and have been corrected for incompleteness and flux bias. Also shown are the cumulative number-count results for the ≈2 Ms CDF-N (dotted curves), the ≈1 Ms CDF-S (red dashed curves; Rosati et al. 2002), the ≈250 ks E-CDF-S (green dash-dotted curves; L05), and *XMM-Newton* observations in the COSMOS field (blue long-dashed curves; Cappelluti et al. 2007). The 2–10 keV fluxes in the ≈1 Ms CDF-S and the COSMOS field were converted to 2–8 keV fluxes assuming a photon index $\Gamma = 1.4$. *Bottom*: Ratio of the CDF-S to CDF-N cumulative number counts for the (*a*) soft band and (*b*) hard band. Ratios were calculated only for number counts that were derived from a sample of $\gtrsim 50$ sources, since for smaller numbers of sources there are large statistical errors. This corresponds to soft-band fluxes $\lesssim 1.5 \times 10^{-15}$ ergs cm^{-2} s^{-1} and hard-band fluxes $\lesssim 5 \times 10^{-15}$ ergs cm^{-2} s^{-1}.

Hasinger, G., Burg, R., Giacconi, R., Schmidt, M., Trumper, J., & Zamorani, G. 1998, A&A, 329, 482
Hornschemeier, A. E., et al. 2001, ApJ, 554, 742
—. 2003, AJ, 126, 575
—. 2004, ApJ, 600, L147
Jerius, D., Donnelly, R. H., Tibbetts, M. S., Edgar, R. J., Gaetz, T. J., Schwartz, D. A., Van Speybroeck, L. P., & Zhao, P. 2000, Proc. SPIE, 4012, 17
Kim, M., et al. 2007, ApJS, 169, 401
Kraft, R. P., Burrows, D. N., & Nousek, J. A. 1991, ApJ, 374, 344
Le Fèvre, O., et al. 2004, A&A, 428, 1043
Lehmer, B. D., Brandt, W. N., Hornschemeier, A. E., Alexander, D. M., Bauer, F. E., Koekemoer, A. M., Schneider, D. P., & Steffen, A. T. 2006, AJ, 131, 2394
Lehmer, B. D., et al. 2005, ApJS, 161, 21 (L05)
—. 2008, ApJ, 681, 1163
Lyons, L. 1991, Data Analysis for Physical Science Students (Cambridge: Cambridge Univ. Press)
Maccacaro, T., Gioia, I. M., Wolter, A., Zamorani, G., & Stocke, J. T. 1988, ApJ, 326, 680
Markevitch, M. 2001, CXC Memo, (Cambridge: CXC) http://cxc.harvard.edu/cal/calreview/mm_calrev_bg.ps
Markevitch, M., et al. 2003, ApJ, 583, 70
Marshall, F. E., Boldt, E. A., Holt, S. S., Miller, R. B., Mushotzky, R. F., Rose, L. A., Rothschild, R. E., & Serlemitsos, P. J. 1980, ApJ, 235, 4
Mignoli, M., et al. 2005, A&A, 437, 883
Mobasher, B., et al. 2004, ApJ, 600, L167
Moretti, A., Campana, S., Lazzati, D., & Tagliaferri, G. 2003, ApJ, 588, 696
Paolillo, M., Schreier, E. J., Giacconi, R., Koekemoer, A. M., & Grogin, N. A. 2004, ApJ, 611, 93
Popesso, P., et al. 2008, A&A, submitted
Ravikumar, C. D., et al. 2007, A&A, 465, 1099
Rosati, P., et al. 2002, ApJ, 566, 667
Stark, A. A., Gammie, C. F., Wilson, R. W., Bally, J., Linke, R. A., Heiles, C., & Hurwitz, M. 1992, ApJS, 79, 77
Stocke, J. T., Morris, S. L., Gioia, I. M., Maccacaro, T., Schild, R., Wolter, A., Fleming, T. A., & Henry, J. P. 1991, ApJS, 76, 813
Szokoly, G. P., et al. 2004, ApJS, 155, 271
Townsley, L. K., Broos, P. S., Garmire, G. P., & Nousek, J. A. 2000, ApJ, 534, L139
Townsley, L. K., Broos, P. S., Nousek, J. A., & Garmire, G. P. 2002, Nuclear Instruments and Methods in Physics Research A, 486, 751
Tozzi, P., et al. 2001, ApJ, 562, 42
Vanzella, E., et al. 2008, A&A, 478, 83
Vikhlinin, A. 2001, CXC Memo, (Cambridge: CXC) http://cxc.harvard.edu/cal/Acis/Cal_prods/vfbkgrnd/
Wolf, C., et al. 2004, A&A, 421, 913
Yang, Y., Mushotzky, R. F., Barger, A. J., Cowie, L. L., Sanders, D. B., & Steffen, A. T. 2003, ApJ, 585, L85

TABLE 1
JOURNAL OF *Chandra* DEEP FIELD-SOUTH OBSERVATIONS

Obs. ID	Obs. Start (UT)	Exposure Time[a] (ks)	Aim Point[b] α (J2000.0)	Aim Point[b] δ (J2000.0)	Roll Angle[c] (deg)	Obs. Mode[d]	Pipeline Version[e]
1431-0.....	1999 Oct 15, 17:38	24.6	03 32 29.44	–27 48 21.8	47.3	VF	R4CU5UPD11
1431-1.....	1999 Nov 23, 02:30	93.6	03 32 29.44	–27 48 21.8	353.9	F	R4CU5UPD11
441.....	2000 May 27, 01:18	56.0	03 32 26.91	–27 48 19.4	166.7	F	7.6.10
582.....	2000 June 03, 02:38	130.6	03 32 26.97	–27 48 18.5	162.9	F	7.6.10
2406	2000 Dec 10, 23:35	29.7	03 32 28.33	–27 48 36.5	332.2	F	7.6.10
2405	2000 Dec 11, 08:14	59.6	03 32 28.82	–27 48 43.5	331.8	F	7.6.10
2312	2000 Dec 13, 03:28	123.7	03 32 28.28	–27 48 36.9	329.9	F	7.6.10
1672	2000 Dec 16, 05:07	95.1	03 32 28.73	–27 48 44.5	326.9	F	7.6.10
2409	2000 Dec 19, 03:55	69.0	03 32 28.08	–27 48 38.6	319.2	F	7.6.10
2313	2000 Dec 21, 02:08	130.4	03 32 28.08	–27 48 38.6	319.2	F	7.6.10
2239	2000 Dec 23, 17:28	130.8	03 32 28.08	–27 48 38.6	319.2	F	7.6.10
8591	2007 Sep 20, 05:26	45.4	03 32 28.20	–27 48 06.9	72.7	VF	7.6.11.1
9593	2007 Sep 22, 20:34	46.4	03 32 28.20	–27 48 06.9	72.7	VF	7.6.11.1
9718	2007 Oct 03, 13:56	49.4	03 32 28.61	–27 48 07.4	62.0	VF	7.6.11.1
8593	2007 Oct 06, 02:04	49.5	03 32 28.61	–27 48 07.4	62.0	VF	7.6.11.1
8597	2007 Oct 17, 07:07	59.3	03 32 29.25	–27 48 10.4	44.2	VF	7.6.11.2
8595	2007 Oct 19, 14:16	115.4	03 32 29.35	–27 48 11.2	41.2	VF	7.6.11.2
8592	2007 Oct 22, 12:14	86.6	03 32 29.62	–27 48 13.8	32.4	VF	7.6.11.2
8596	2007 Oct 24, 13:20	115.1	03 32 29.62	–27 48 13.8	32.4	VF	7.6.11.2
9575	2007 Oct 27, 05:43	108.7	03 32 29.62	–27 48 13.8	32.4	VF	7.6.11.2
9578	2007 Oct 30, 22:35	38.6	03 32 29.84	–27 48 16.7	24.2	VF	7.6.11.2
8594	2007 Nov 01, 11:51	141.4	03 32 29.84	–27 48 16.7	24.2	VF	7.6.11.2
9596	2007 Nov 04, 04:11	111.9	03 32 29.95	–27 48 18.5	19.8	VF	7.6.11.2

NOTE. — The focal-plane temperature was −110°C during the first two observations and −120°C during the others. Units of right ascension are hours, minutes, and seconds, and units of declination are degrees, arcminutes, and arcseconds.
[a] All observations were continuous. The data were filtered on good-time intervals, and one mild flare was removed in observation 1431-0. The short time intervals with bad satellite aspect are negligible and have not been removed. The total exposure time for the 23 observations is 1.911 Ms.[b] The average aim point, weighted by exposure time, is $\alpha_{J2000.0} = 03^h32^m28\overset{s}{.}80$, $\delta_{J2000.0} = -27°48'23\overset{''}{.}0$.[c] Roll angle describes the orientation of the *Chandra* instruments on the sky. The angle is between 0–360°, and it increases to the west of north (opposite to the sense of traditional position angle).[d] The observing mode: F=Faint mode and VF=Very Faint mode.[e] The version of the CXC pipeline software used for basic processing of the data.

TABLE 2
MAIN *Chandra* CATALOG

	X-ray Coordinates				Counts					
No. (1)	α_{2000} (2)	δ_{2000} (3)	Pos Err (4)	Off-Axis (5)	FB (6)	FB Upp Err (7)	FB Low Err (8)	SB (9)	SB Upp Err (10)	SB Low Err (11)
1 ...	03 31 34.19	–27 50 04.2	1.6	12.19	26.1	11.1	11.8	13.5	–1.0	–1.0
2 ...	03 31 35.79	–27 51 34.7	1.9	12.14	14.9	–1.0	–1.0	12.1	7.3	7.2
3 ...	03 31 40.15	–27 47 46.3	1.3	10.77	33.6	11.8	11.8	25.8	8.4	8.1
4 ...	03 31 40.93	–27 46 21.8	1.1	10.77	61.2	14.0	14.0	16.0	–1.0	–1.0
5 ...	03 31 44.23	–27 49 25.5	1.0	9.91	79.5	19.4	19.4	37.8	12.5	12.5

NOTE. — Units of right ascension are hours, minutes, and seconds, and units of declination are degrees, arcminutes, and arcseconds. Table 2 is presented in its entirety in the electronic edition. An abbreviated version of the table is shown here for guidance as to its form and content. The full table contains 49 columns of information on the 462 X-ray sources.

TABLE 3
SUMMARY OF *Chandra* SOURCE DETECTIONS

Band (keV)	Number of Sources	Detected Counts Per Source Maximum	Minimum	Median	Mean
Full (0.5–8.0)	403	21579.7	11.4	101.0	410.6
Soft (0.5–2.0)	392	15929.7	4.7	53.0	269.9
Hard (2–8)	265	5664.3	7.7	88.6	216.9

TABLE 4
SOURCES DETECTED IN ONE BAND BUT NOT ANOTHER

Detection Band (keV)	Nondetection Energy Band		
	Full	Soft	Hard
Full (0.5–8.0)	...	67	141
Soft (0.5–2.0)	56	...	166
Hard (2–8)	3	39	...

NOTE. — For example, there were 67 sources detected in the full band that were not detected in the soft band.

TABLE 5
SUPPLEMENTARY CDF-S PLUS E-CDF-S *Chandra* CATALOG

	X-ray Coordinates				Counts					
No. (1)	α_{2000} (2)	δ_{2000} (3)	Pos Err (4)	Off-Axis (5)	FB (6)	FB Upp Err (7)	FB Low Err (8)	SB (9)	SB Upp Err (10)	SB Low Err (11)
1 ...	03 31 40.98	–27 44 34.8	1.0	11.24	118.4	12.8	11.6	56.1	8.8	7.7
2 ...	03 31 42.76	–27 53 40.7	1.6	11.47	17.4	5.9	4.7	7.5	4.2	3.0
3 ...	03 31 43.21	–27 54 05.1	0.9	11.58	152.3	14.2	13.1	49.7	8.4	7.3
4 ...	03 31 44.64	–27 45 19.1	1.2	10.23	39.9	8.1	6.9	7.5	–1.0	–1.0
5 ...	03 31 48.14	–27 52 32.1	1.6	9.90	10.8	–1.0	–1.0	8.1	4.4	3.2

NOTE. — Units of right ascension are hours, minutes, and seconds, and units of declination are degrees, arcminutes, and arcseconds. Table 5 is presented in its entirety in the electronic edition. An abbreviated version of the table is shown here for guidance as to its form and content. The full table contains 52 columns of information on the 86 X-ray sources.

TABLE 6
SUPPLEMENTARY OPTICALLY BRIGHT *Chandra* CATALOG

	X-ray Coordinates				Counts					
No. (1)	α_{2000} (2)	δ_{2000} (3)	Pos Err (4)	Off-Axis (5)	FB (6)	FB Upp Err (7)	FB Low Err (8)	SB (9)	SB Upp Err (10)	SB Low Err (11)
1 ...	03 31 50.82	–27 47 03.8	1.2	8.50	47.2	–1.0	–1.0	22.1	5.8	4.7
2 ...	03 31 52.03	–27 50 37.6	1.2	8.43	40.9	–1.0	–1.0	20.8	5.6	4.5
3 ...	03 31 57.23	–27 45 36.9	1.2	7.51	41.6	–1.0	–1.0	22.7	5.8	4.7
4 ...	03 32 00.32	–27 46 11.4	1.2	6.67	35.9	–1.0	–1.0	18.7	5.4	4.3
5 ...	03 32 06.59	–27 50 37.3	1.2	5.39	24.3	–1.0	–1.0	12.0	4.6	3.4

NOTE. — Units of right ascension are hours, minutes, and seconds, and units of declination are degrees, arcminutes, and arcseconds. Table 6 is presented in its entirety in the electronic edition. An abbreviated version of the table is shown here for guidance as to its form and content. The full table contains 38 columns of information on the 30 X-ray sources.

TABLE 7
BACKGROUND PARAMETERS

Band (keV)	Mean Background		Total Background[c]	Count Ratio[d]
	(counts pixel^{-1})[a]	(counts Ms^{-1} pixel^{-1})[b]	(10^5 counts)	(background/source)
Full (0.5–8.0)	0.248	0.242	16.1	9.7
Soft (0.5–2.0)	0.067	0.066	4.3	4.1
Hard (2–8)	0.179	0.167	11.6	20.2

[a] The mean numbers of background counts per pixel. These are measured from the background images described in §4.[b] The mean numbers of counts per pixel divided by the mean effective exposure. These are measured from the exposure maps and background images described in §4.[c] Total number of background counts.[d] Ratio of the total number of background counts to the total number of source counts.